9-10-2010

Sintering of metal nanoparticles on model substrates

Levi R. Houk

Levi R. Houk
Candidate

Chemical & Nuclear Engineering
Department

This thesis is approved, and it is acceptable in quality and form for publication:

Approved by the Thesis Committee:

_____ ,Chairperson

_____

_____

Sintering of Metal Nanoparticles on Model Substrates

by

Levi Read Houk

B.S. Chemical Engineering, Kansas State University 2007

THESIS

Submitted in Partial Fulfillment of the

Requirements for the Degree of

Master of Science
Chemical Engineering

The University of New Mexico

Albuquerque, New Mexico

July, 2010

Dedication

To my family, without their encouragement and support, none of this would have been possible.

Acknowledgments

I am grateful to my advisor, Dr. Abhaya Datye, for his continued support, encouragement, and guidance throughout the course of my studies, for accepting me as an undergraduate researcher for one summer as an REU and for showing that simple solutions are not always that simple and that difficult solutions are not nearly that difficult.

Special thanks are for Sivakumar Challa, who programed the deterministic models and developed the atomistic Monte Carlo Simulations and enlightened me with many long conversation and taught me new ways about thinking about research and tackling complicated problems. And for Ron Goeke who deposited the Pd on the single crystals at Sandia National Lab and helped with the focused ion beam on the single crystal samples. And to my two undergraduate students, Angelica Sanchez and Amanda Staker, for teaching me patience and how to explain how to do research and why we do it, and for making me a better researcher myself.

I would also like to thank the members of the Datye research group; Patrick Burton, Amanda Staker, Angelica Sanchez, Jonathan Piaz, Eric Peterson, Ron Goeke, Barr Halevi, Hien Pham, Sivakumar Challa and former members for their guidance and advice; Andrew DeLaRiva, John Gabaldon, and Travis Conant .

I would like to acknowledge the financial support of this work from the U.S. National Science Foundation GOALI (Grant Opportunities for Academic Liaison with Industry) grant CTS 05-00471 and also through the U.S. National Science Foundation PIRE (Partnership for International Research & Education) grant OISE 0730277. The work made use of the electron microscopy facilities at the University of New Mexico which are supported by the NSF EPSCOR and NSF NNIN grants.

Also my committee, Dr. Abhaya Datye (chair), Dr. Dimiter Petsev, and Dr. Boris Kiefer.

Sintering of Metal Nanoparticles on Model Substrates

by

Levi Read Houk

ABSTRACT OF THESIS

Submitted in Partial Fulfillment of the

Requirements for the Degree of

Master of Science

Chemical Engineering

The University of New Mexico

Albuquerque, New Mexico

July, 2010

Sintering of Metal Nanoparticles on Model Substrates

by

Levi Read Houk

B.S. Chemical Engineering, Kansas State University 2007

M.S., Chemical Engineering, University of New Mexico, 2010

Abstract

The sintering of precious metal catalyst is an important problem for the automative and chemical process industry. As these precious metal catalyst sinter, the metal nanoparticles grow, this in return causes a loss in the overall surface area from losing the number of available reaction sites. At high temperatures, sintering as a thermally activated process occurs more rapidly and the energetics of the sample changes. In automotive catalyst, for the catalytic converter, the exhaust gases from automobiles contain carbon monoxide, nitrogen oxide compounds, other hydrogen compounds, are detrimental to the atmosphere and a catalyst is required to convert these gasses into less harmful gases, such as nitrogen, carbon dioxide, and water vapor. These reactions occur at very high temperatures, greater than $900\,^{\circ}\mathrm{C}$, which causes the catalyst to degrade and not be as effective in converting these harmful gases to less harmful gases, requiring some state governments to mandate the testing of the exhaust gases from cars periodically to ensure the proper conversion is occurring. Despite the importance of catalyst sintering, there is much yet to be under-

stood about the mechanism of how catalyst sinter and to predict catalyst lifetimes under operating conditions.

To better study how sintering occurs, single crystal model catalyst will be employed for my experiments. A palladium catalyst, one of the three metals used in catalytic converters, was deposited on the single crystal metal-oxide substrates. The three metal-oxides examined were Pd on α-alumina, quartz (silica), and yttria stabilized zirconia. Palladium nanoparticles with an average size of around 15 nm were created from a thin film of deposited pure palladium. After the creation of palladium nanoparticles, the samples were aged under two different conditions, under a vacuum atmosphere and a nitrogen atmosphere. The vacuum atmosphere is used to measure the emission of adatoms from the nanoparticles. Any adatom emitted from the particle into the atmosphere will be removed from the system, causing a loss of mass to the system. The mass loss can be measured indirectly by using a scanning electron microscope and analyzing images of the system to calculate the mass lost from the system. From this mass loss, we can calculate the emission rate of Pd on the different supports to see how the support affects the emission of adatoms.

Then other ageing condition is in nitrogen, where there would be no mass loss in the system, and from the scanning electron microscope we can analyze how rapidly particles grow. The faster the particles grow, then the sintering rate is greater, most likely from a greater rate of adatom emission. If the sintering rates correlate to emission rates under vacuum, then the emission step is critical to the understanding of catalyst sintering.

My research shows that the support does affect the emission and sintering rates. Results of evaporation at $900\,^{\circ}\mathrm{C}$ under vacuum showed the Pd on α-alumina evaporated the least, followed by Pd on YSZ then Pd on quartz. The results of sintering at $700\,^{\circ}\mathrm{C}$ showed that these trends also were true for sintering rates, with Pd on alumina sintering the least followed by Pd on YSZ and then Pd on quartz. These results show that the emission of adatoms can be measured by vacuum and the sintering rates do correlate. With the emis-

sion rates correlating, there might be ways to learn to learn how the support affects the amount of sintering. This might lead to the better design of catalysts which might reduce the amount of sintering.

Contents

List of Figures

List of Tables

Glossary

SEM	Scanning Electron Microscopy uses a focused electron beam (usually low energy, 2-20 kV) to image a sample. The two imaging modes used in this study are secondary electron (SE) which gives surface information and backscattered electron (BSE) which has contrast with respect to the atomic weight (Z) of the sample.
FIB	Focused Ion Beam is an imaging and etching tool similar to an SEM, but unlike the SEM, it emits electrons and ions to the sample. The ions in this case were Ga ions which was used to etch patterns into the surface.
VTZ	Vacuum Time Zero is the method to create nanoparticles from a thin film of metal through heating up the sample in vacuum after the thin film had been oxidized. Heating the sample in vacuum allowed for the oxygen to dewet the metal and create nanoparticles on the surface.
YSZ	YSZ is Yttria Stabilized Zirconia, a metal-oxide support used in this study. This support is zirconia stabilized with 8 wt% yttria.

Chapter 1

Introduction

1.1 Introduction to Catalyst

A catalyst is a material which plays a role in a chemical reaction where it lowers the activation energy barrier for the reactants to progress towards the products. There are two types of catalyst, homogenous catalyst, where the catalyst is in the same phase as the reactants, and heterogenous catalyst, where the catalyst is a different phase than the reactants. Heterogenous catalyst, which are the focus of this study, are commonly used in industry where the catalyst is in a form of a solid and the reactants and products are in the gas or liquid phase as they react on the catalyst. Catalyst commonly consist of noble metals, such as platinum, palladium, silver, and gold. Other non-noble metals used for catalyst are copper, nickel and iron. These metals are expensive with noble metals being the most expensive. A support is used for the metal catalyst to keep the catalyst as small particles to provide a framework and structure for the catalyst to sit in, as opposed to just using the bulk metal as the catalyst. Catalyst supports are generally a high surface area material, either carbon, an inexpensive metal, or a metal oxide.

1.2 Catalyst Deactivation

Deactivation of catalyst may occur by poisoning, coking or sintering. Poisoning of a catalyst typically occurs where a chemical species absorbs very strongly onto a catalyst site and will not desorb at reaction conditions. This reduces available sites from the reaction and decreases the reaction rate. An example of this behavior for the petrochemical cracking reactions with small amounts of sulfur, with the sulfur bonding strongly to a typical platinum catalyst which slowly deactivates the catalyst. Coking is where carbon deposits from a chemical reaction will build up on the catalyst taking away active sites. For both coking and poisoning, the catalyst must be heated to very high temperatures to burn of the chemicals contaminating the catalyst. Sintering is another mechanism by which catalysts deactivate. In this process, smaller particles will loose mass to larger particles, Figure 1.1. As sintering occurs, available reaction sites are lost from the loss as the number of smaller particles either ripen to larger particles or migrate and coalesce to form larger particles. The reaction sites which were on the surface of the smaller particles are now in the bulk of the larger particles, not being available to participate in the reaction.

1.3 Motivation

Catalysts play an important role in the chemical manufacturing industry, automotive industry and the pollution prevention industry. It is estimated that more than 90% of all chemical manufacturing involves a catalyst [5]. More specifically, catalyst are used in the catalytic converter in automobiles to clean carbon monoxide, nitrous oxides, and hydrocarbons from the exhaust into more environmentally friendly and less toxic gases. As these catalyst are used, they deactivate over time and the catalyst becomes less effective. At high temperatures, where some chemical reactions occur, the sintering mode of deactivation is enhanced, this leads to a rapid loss of catalytically active sites. Even though this process

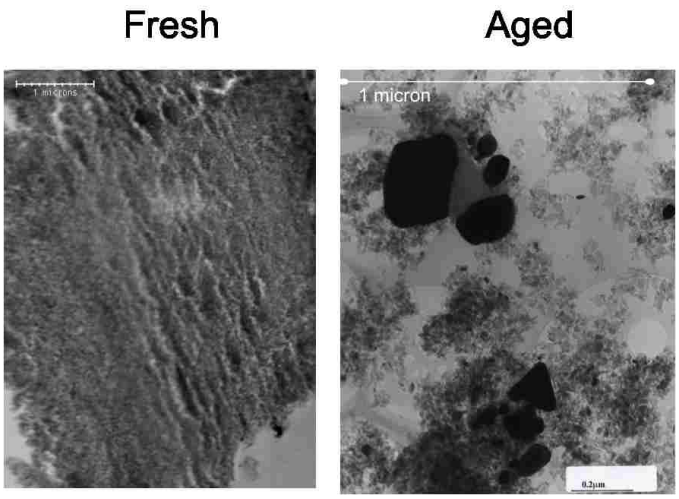

Figure 1.1: A supported Pt catalyst, left, a fresh catalyst, right, after the catalyst has been aged there are larger Pt particles

is important to several industries, there is a lack of fundamental understanding on how sintering occurs and systematic ways to prevent it.

1.4 Problem Statement

Since catalysts deactivate over time, which creates a loss of available surface reaction sites, the reactivity of the catalyst also decreases. If the deactivation mechanism is better understood or possibly controlled, the process of deactivation, via the sintering mechanism, could be controlled or even possibly stopped or reserved. In literature, studies by Exxon [6] have shown evidence for the redispersion of Ir nanoparticles with the addition of Group IIA metals-oxides (BaO, CaO, SrO) to the alumina support. This redispersion could lead to controlling or reversing catalyst sintering with a better understanding of how particles ripen, catalyst could be synthesized to enhance redispersion.

Examining sintering on model catalyst, as opposed to industrial catalyst, eliminates

complications of having to deal with the pores that may influence sinteirng and allows for the same sample, and in some cases, the same region of the sample, before and after ageing. Model substrates also allow us to to studying sintering under different kinds of conditions more easily, including studying catalyst under vacuum, allowing the measurement of the emission of adatoms directly from the nanoparticle, and then correlate emission rates to sintering rates on model catalyst under high temperatures and inert atmospheres.

1.5 Hypothesis

From the ripening mechanism of sintering, there are two possible rate limiting steps, the emission of the adatom and the diffusion of the adatom along the substrate. Assuming that the adatoms diffuse across the substrate easily and that the emission of adatoms is the most energy intensive step in ripening, would make the process emission limiting. If the differences in sintering rates are caused by the differing rates of emission of adatoms from the metal particles along the substrate, then the rates of sintering could linked by measuring the emission of adatoms from the nanoparticles. By measuring the emission rates by using the SEM and observing how particles evaporate under vacuum ageing conditions, the emission rates can be quantified.

Chapter 2

Literature and Background

2.1 Theory of Sintering

Sintering of nanoparticles occurs via two mechanisms, in Figure 2.1. One is the coalescence of the metal nanoparticles that are mobile on the support and the other is the ripening of smaller particles to the more energy favorable, larger particles. Both processes occur during sintering conditions, to varying degrees. Each will be examined in detail in the following subsections.

Theory of Coalescence

The process of coalescence is limited by the process of particle diffusion, where it is believed that small particles can diffuse across the substrate when adatoms on one side of a particle are diffusing on the substrate very rapidly and frequently, allowing for the small particle to be mobile on the support. This process is referred to as Brownian motion where the adatoms are diffusing fast enough for the particle to migrate across the surface one atomic diameter at a time. The particles that are mobile on the substrate have a probability

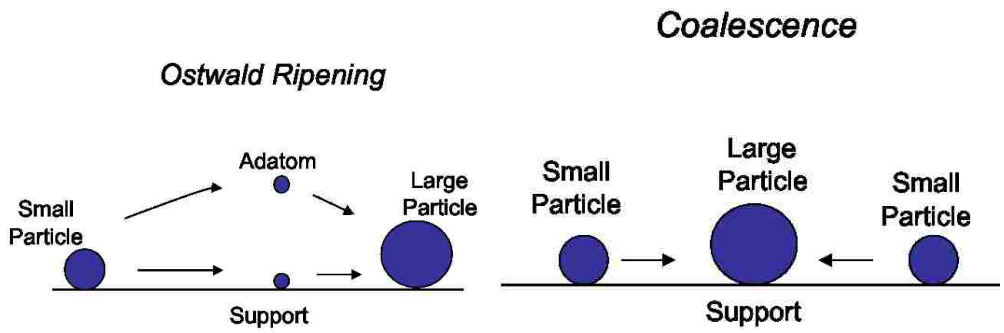

Figure 2.1: Illustration depicting the mechanism of Ostwald Ripening (left). Illustration showing the small particle mobile on the substrate colliding into a larger particle, the mechanism of Coalescence (right).

of encountering another particle, either stationary or mobile, where the two particles meet and coalesce and form one larger particle [7].

The process of coalescence is divided into three steps. The first step is when the two particles are extremely close and neck growth occurs. Neck growth is when the two particles are still distinctly visible yet there is a connecting bridge between the particles. After some duration of time, the neck elimination step occurs, this is when the two particles are still centered in their respected positions in the neck growth stage, however, the neck is no longer present and the single particle that is observed from the two original particles is an elongated particle. After more time, the particle reconfigures from the neck elimination step to complete coalescence. This is when the particle is back to the most energy favorable configuration, whether it is a spherical or faceted particle [7].

Previous work shows that the method of sintering by analyzing the particle size distribution. For coalescence, it was predicted by Granqvist and Buhrmann [8] that a log normal distribution, Figure 2.2 [1], would arise if you were starting with a symmetric Gaussian-shaped distribution. With a log normal distribution, small particles do remain with a large peak of small particles are still present, but a tail of large particles develops. These large

particles that are present in the tail are from particle coalescence events when the smaller particles collide with another particle, causing rapid growth of large particles. Since the coalescence events may not occur too frequently, the tail does not contain many particles.

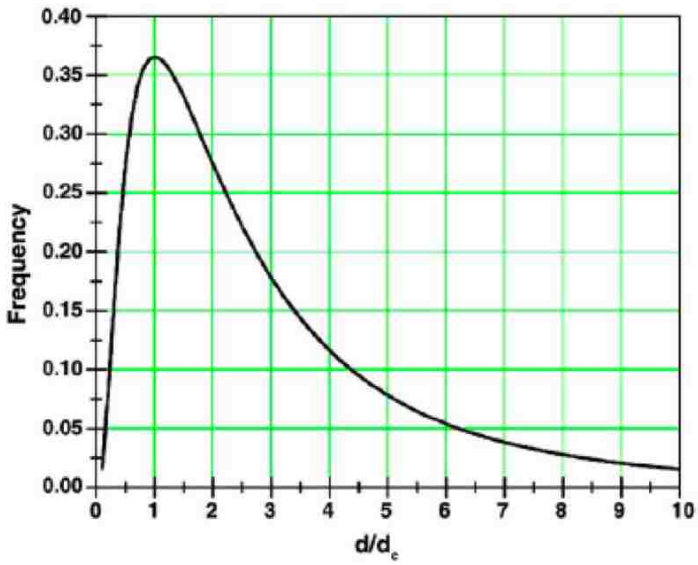

Figure 2.2: The expected particle size distribution from coalescence sintering events, a Log Normal distribution, based on the theory by Granqvist and Buhrmann, plot from Datye et. al. [1]

Theory of Ostwald Ripening

The other method of sintering is the ripening of particles. This is a much slower sintering process than coalescence. This mechanism of sintering involves the depletion and addition of single adatoms to or from the surface to the particle. For Ostwald ripening to occur, an atom on the particle must overcome energy barriers to become a ”monomer on the particle”, or an atom that is bound to both the particle and the substrate, then the atom overcomes the energy barrier to become detached from the particle and onto the substrate. Once the atom is on the substrate it goes from site to site until it it reaches another particle,

a larger energitically more favorable, and reattaches to the particle. In order for particles to grow these events must happen many times. As these events increase in number, the smaller particles get smaller and the large particles slowly get larger.

The predicted particle size distribution from the coarsening of particles is a LSW type distribution, predicted independently by both Lifshitz and Slyozov [2] and also by Wagner [3] (LSW). This particle size distribution, Figure 2.3 [1], has a peak over larger particles with a tail towards smaller particles as a result of smaller particles ripening away to the larger particles. Larger particles are stable and are slowly growing but small particles are quickly being depleted by loosing atoms through the ripening process until they are small enough to not support any atoms and vanish.

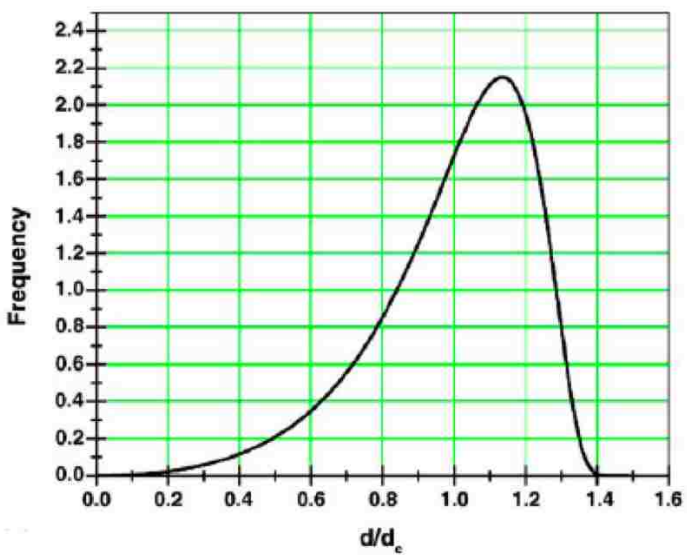

Figure 2.3: The expected particle size distribution from Ostwald Ripening sintering events, a LSW distribution, based on the theory by both Lifshitz and Slyozov (LS) [2] and also by Wagner (W)[3], plot from Datye et. al. [1]

2.2 Evidence of Ostwald Ripening Sintering

In recent experiments published in the literature gives evidence of ripening being the dominant sintering mechanism. First, the work of Goeke and Datye [4] investigating Pd on model quartz substrates showed that ripening was the dominant sintering mechanism. Using a scanning electron microscope (SEM) to view the same region on the planar quartz support before and after ageing the sample in an atmosphere of 600 Torr N_2 at $900\,^{\circ}\mathrm{C}$ at time intervals of 0.3 and 12 hours showed that large particles were stationary but smaller particles around these larger particles were slowly shrinking or they were no longer present. Seeing the smaller particles decrease over time indicates that the ripening mechanism is present over the coalescence mechanism.

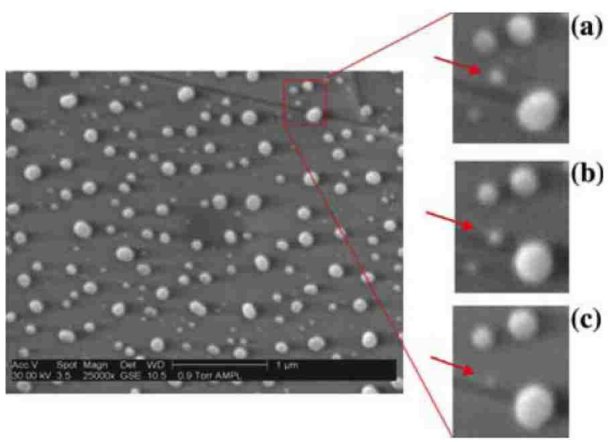

Figure 2.4: ESEM image of a Pd on quartz wafer aged at $900\,^{\circ}\mathrm{C}$ in nitrogen, each image on the right were taken during the ageing, (a) at time = 0 hr (b) at time = 0.3 hr and (c) at time = 12 hr. This shows small particles ripening during the aging, figure from Goeke et. al.[4]

Another study showing ripening was performed by Goodman's group at Texas A&M on gold nanoparticles on model TiO_2 (110) support during the carbon monoxide (CO) oxidation reaction [9]. It has been shown that gold sinters readily under CO oxidation condi-

tions and gold nanoparticles less than 5 nm are needed for reactivity. For this work, they used *in-situ* scanning tunneling microscopy (STM) with reaction condition of a temperature between 300 and 410 K and a total pressure of 0.1 Torr. They viewed gold nanoparticles that could be seen to ripen under reaction conditions while the larger, more stable particles were immobile on the support.

Work at Arizona State University by Crozier's group on a Pd on alumina powder catalyst using environmental transmission electron microscopy (ETEM) with conditions of 500 mTorr of steam at $700\,^{\circ}\mathrm{C}$ and also at $350\,^{\circ}\mathrm{C}$ [10]. At elevated temperatures, they observed both ripening and coalescence occurring, but to differing extents, the ripening mechanism occurred more frequently than the coalescence events. At the lower temperatures, ripening was also the main mechanism of sintering.

In a mesoporous support study with gold in mesoporous silica, it was shown that by encapsulating the gold nanoparticles, the mobility of the particles could be suppressed [11]. This study heated the gold on silica up to $400\,^{\circ}\mathrm{C}$ during the exothermic CO oxidation reaction. This study found that the mesoporous silica improved the thermal stability of gold and help minimize the amount that gold sinters.

2.3 Support Dependence on Sintering

The sintering rates of a metal supported catalyst is support dependent [12]. A study of the sintering kinetics of nickel supported on both silica and alumina substrates reveal that under a hydrogen atmosphere, the sintering rates for nickel on silica is far greater than that of nickel on alumina. With a similar weight loading of nickel, 13.5 wt% on silica and 15.0 wt% on alumina, and heating the catalyst at either 923, 973, or 1023 K showed that nickel on silica lost active sites at a much higher rate than that of nickel on alumina. This study gives evidence that sintering is support dependent, but gives little information on why a

catalyst on one support would sinter differently on another support.

2.4 Evaporation Studies of Metallic Nanoparticles

The evaporation rate of a metallic film was first related to the vapor pressure of the metal in 1913 [13]. However, with nanoparticles, the curvature of the particles must be accounted for. The Gibbs-Thomson equation accounts for particle curvature for metal evaporation. This was verified by *in-situ* TEM of Pb nanoparticles on carbon [14]. Lisgarten et. al. experimentally showed that the evaporation of Pb and Au nanoparticles on a carbon support fitted the Gibbs-Thomson equation, while assuming constant metal surface interfacial energies. Proving that the method of evaporation is direct evaporation from the nanoparticle surface.

In other studies, by the Beke group, they deposited an 8 to 20 nm thin film of Cu on Molybdenum [15] or a Pd film on sapphire [16] and studied evaporation via auger electron spectroscopy or atomic force microscopy. For both samples, they observed evaporation greatly exceeding, by an order of magnitude, above what would be expected over direct evaporation from the nanoparticles. Their results were more in line with what would be expected from a thin film evaporating, suggesting that evaporation was occurring via a surface diffusion of metal adatoms on the substrate and evaporation was occurring from the adatom species on the substrate and not significantly from the particles. From this, they could find the rates of diffusion from measuring evaporation.

2.5 Fundamental Studies of Catalyst Sintering Using Moldel Catalyst

Model substrates have also been used to understand sintering since the 1970's when Wynblatt and Gjostein [7] used model catalyst to understand mechanisms of sintering for the Ford Motor Company using TEM. Also, in the 1970's McVicker [6] used model studies to help support experimental evidence of Ir on Alumina sintering and the redispersion of catalyst for Exxon.

In more recent work, since the 1990's, two groups have excelled at using single crystal studies to learn about the fundamentals of catalyst sintering, these are the groups of Wayne Goodman at Texas A&M and Charlie Campbell at the University of Washington. Goodman's group has been a pioneer into the surface science understanding of catalyst [17]. Most of their work has been directed at understanding the activity [18] and stability of gold catalyst [9] and the nature of their binding sites on TiO_2 surfaces [19]. Goodman's group has also has used model catalyst to understand the behavior of bimetallic catalyst [20, 21] and also understanding the reactivity of model catalyst of Pt group metals by combing CO Oxidation and STM [22–25].

Charlie Campbell's group also uses single crystal, metal oxide substrates to understand catalyst sintering, they use microcalorimetry to understand energies for sintering and STM or AFM to understand particle size distributions to apply to sintering theory in the literature. Campbell has measured the adsorption energies of Pb with his microcalorimeter [26] and measured how the differences in particle size differed for different sized particles and correlated the size of the particle to the energy of that particle [27], which for small particles is much more than what the Gibbs-Thompson effect predicted. In other work using Au supported on TiO_2, Campbell and Parker improved the sintering model developed by Wynblatt and Gjostien [7] to include the full Gibbs-Thompson term [28].

Chapter 3

Materials and Methods

3.1 Experimental

3.1.1 Evaporation Studies

The YSZ (100) single crystal, the SiO_2 Quartz (x plane out) single crystal, and the Al_2O_3 sapphire (0001) single crystal (all purchased from the MTI Corporation) have the dimensions of 5.0×5.0×0.5 mm with 1 side polished. On the polished surface, a 1.5 nm thin film of Pd (high purity 99.999%) was deposited by electron beam evaporation with a rate of 0.4 Å/min. The amount of Pd was measured by a quartz crystal microbalance to ensure the desired thickness was achieved.

After the thin film of Pd was deposited onto the single crystal, the sample was heated in air to $700\,^{\circ}\mathrm{C}$ for 1 hr with a ramp rate of $20\,^{\circ}\mathrm{C}/\mathrm{min}$ to form a palladium oxide layer on the surface.

This oxidation step roughened up the Pd surface, allowing for easier creation of nanoparticles. To form the nanoparticles, the sample was then heated in a high vacuum atmosphere

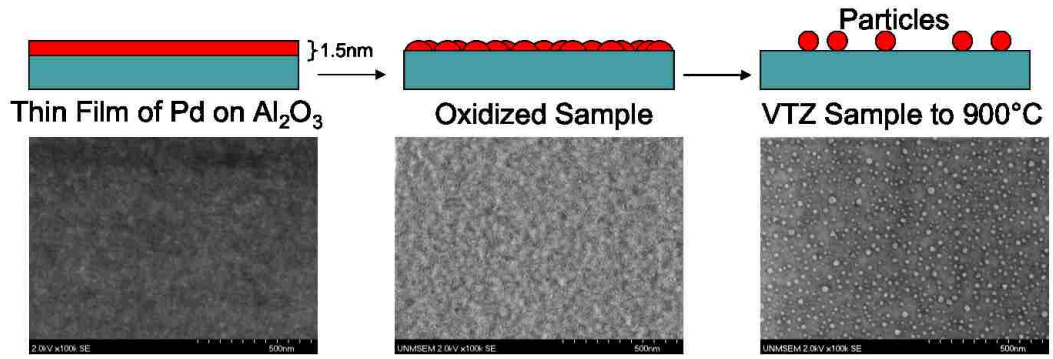

Figure 3.1: Depicting the process called vacuum time zero (VTZ) of creating nanoparticles on a single crystal wafer (top) and SEM micrographs of each step (below).

to $900\,^{\circ}\mathrm{C}$ with a ramp rate of $20\,^{\circ}\mathrm{C}/\mathrm{min}$, as soon as the sample reached $900\,^{\circ}\mathrm{C}$, the heat was removed and the sample was allowed to cool rapidly in a room temperature environment while remaining under vacuum. This step, as seen in Figure 3.1, is referred to as vacuum time zero (VTZ), created nanoparticles on the order of 15 nm and is the initial distribution for our samples, for a more detailed account on this process, refer to Goeke et. al [4].

The high temperature/high vacuum apparatus is comprised of a roughing pump, a high vacuum turbo pump, and a 10 in. long quartz tube that fits inside a tube furnace, Figure 3.2. The sample is placed on a quartz rod that was custom built with a holder that easily fits the single crystal substrates and reaches into the center of the tube furnace. The quartz rod is hollow to allow a thermocouple to hit the rod near where the sample is positioned, to independently measure the temperature to ensure the tube furnace is heating the sample to the desired temperature. The vacuum system is pumped down to at least $1\text{x}10^{-7}$ Torr during the evaporation experiments.

After the initial VTZ step, the samples where imaged with a high resolution scanning electron microscope (SEM). Using the SEM at low accelerating voltages allowed us to see the surface of the substrates in great detail and allowed us to clearly distinguish the

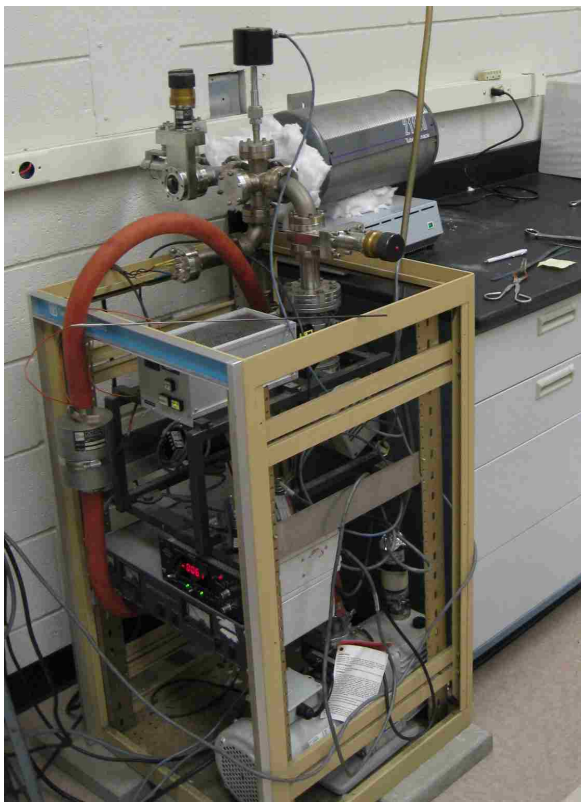

Figure 3.2: Picture of the high vacuum setup with the heater on the quartz tube.

Pd nanoparticles and the single crystal substrate substrate. Imaging on the SEM could be done with either secondary electrons (SE) or with back scattering electrons (BSE). Secondary electrons obtained with the SEM give the features of the substrate and allow us to see particles above 5 nm with the high resolution imaging. Backscattered electrons allow for z-contrast imaging, easily distinguishing between the heavy metallic particles and the much lighter oxide substrates. The SEM used is a Hitachi S-5200 Nano SEM, with a resolution at 1 kV of 1.7 nm.

The process for analyzing the SEM images, as seen in Figure 3.3 left, began with using software, such as PCI Quartz or Adobe Photoshop, to crop the micrograph to remove the scale bar but to preserve all of the original information in the image. Then the cropped

micrograph was brought into the PGT Spirit Software, where it was first calibrated for the magnification that the image was taken, to insure that the correct ratio of length in nm to pixels in the micrograph are correct. Then the image is passed through a medium filter to clean up noise as a result from the metal oxide substrate charging under the electron beam or other noise from the electron imaging. Then the grayscale micrograph is then converted into a binary micrograph, Figure 3.3 center, where the blue pixels are the brighter regions of the sample, usually particles, and the black regions are the darker regions of the sample, indicating the substrate.

This binary micrograph is then subjected to a feature analysis where the blue pixels are then grouped together as particles and tabulated with a few restrictions, particles on the edge are not counted, along with very irregularly shaped particles are also not counted, and particles that are less than 4 nm in diameter are not counted because they may be noise. This feature analysis then presents the results Microsoft Word and Excel documents including all the statistical information of the sample and the particle diameter of each particle counted. A new micrograph is created after the feature analysis is performed, Figure 3.3 right, where it displays the particles counted, indicated by white particles, and particles that were not counted, blue particles. As seen in Figure 3.3 right, only a few particles are not counted, there are only a few particles on the edge, which would lead to counting of incomplete particles, and only a few particles not counted due to size, which may or may not be particles and could just be noise from the image, none of these are believed to contribute to any error in the analysis.

The samples where then heated in high vacuum at $900\,^{\circ}\mathrm{C}$ for 30 minute increments. The samples were cooled rapidly under vacuum after the ageing, then the samples taken out of the system when they were at room temperature, then the samples were viewed by the SEM and by atomic force microscopy (AFM). This process was repeated until all the Pd had evaporated off of the substrate.

Also, a focused ion beam (FIB) was used to create markings on the single crystal of

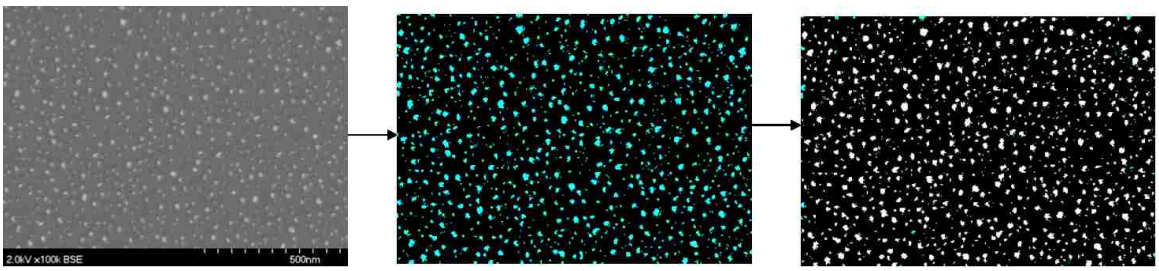

Figure 3.3: Illustrating the process of analysis of SEM imaging, the original image (left), the binary image (center), and the final image after analysis (right).

both YSZ and of Quartz. These markings were etched out with the gallium ion beam. The sample was first coated with chrome to help minimize the effect of the gallium beam on the single crystal sample. The markings consisted of a large cross that would be easily viewed using low magnification or even an optical microscope. This cross lead to near the center of the single crystal, where a 5x5 grid was etched out, Figure 3.4. The dimensions inside each grid was slightly larger than 1 μm x 1 μm, roughly the same size of the typical image taken with the SEM in the non-FIBed samples.

Above and to the side of the FIB grid coordinates were etched, the coordinates consisted of either a letter or a number to ensure that the same position in the grid could be looked at before or after ageing, but unfortunately, the FIB beam was slightly too broad and there may have been some charging of the sample and the letters and numbers were not legible, as seen in Figure 3.5. However, if the sample were to be placed in the sample holder in the identical position each time the sample is inserted into the microscope, the same point of reference could be achieved. This was accomplished by chipping one corner of the wafer and placing it so it would be on the left hand side and furtherest from the microscope. As seen in Figure 3.5, the same area can easily been seen before and after ageing at high temperatures. Also, the FIB markings are stable and do not alter during the high temperate, $900\,^{\circ}\mathrm{C}$, ageing treatments.

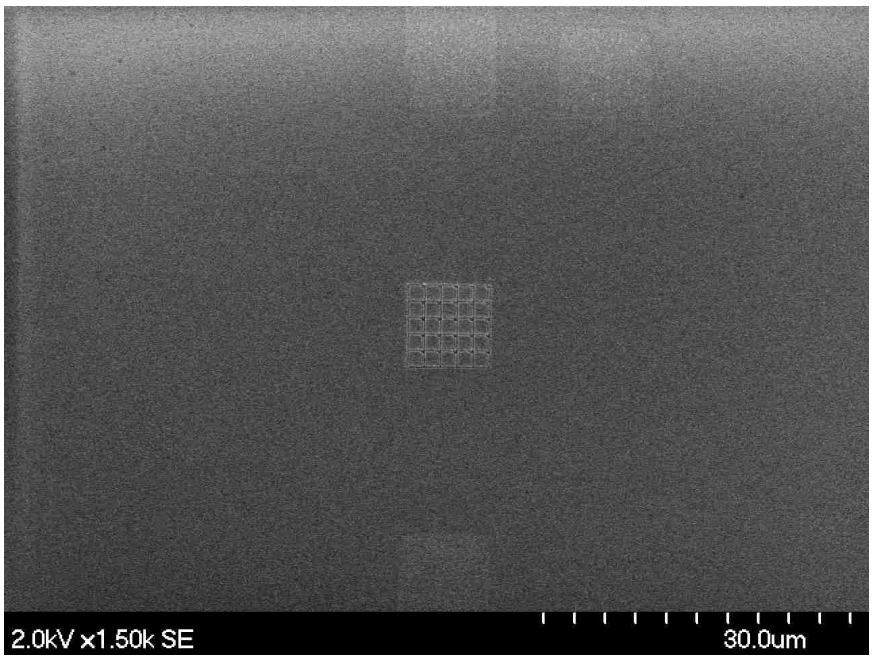

Figure 3.4: The entire FIB grid in a low magnification SEM micrograph that includes the lines that guide to the FIB grid, which can be seen at the top and bottom center of the micrograph.

3.1.2 Sintering Studies

The sintering studies used the same single crystals that were used in the evaporation experiments. Wafers that had 1.5 nm thin film of Pd deposited for the evaporation experiments were also prepared in the same batch for the sintering studies. The wafers should be nearly identical for both the sintering and evaporation experiments.

Palladium nanoparticles were created using two different methods for the sintering studies. One is the same exact process that was used for the VTZ step in the evaporation studies, where the Pd was oxidized in air then heated up in high vacuum to $900\,^{\circ}\mathrm{C}$. However, for the sintering experiments, taking the Pd nanoparticles and the single crystal wafers to such high temperatures proved to cause some surface defects to the single crystal

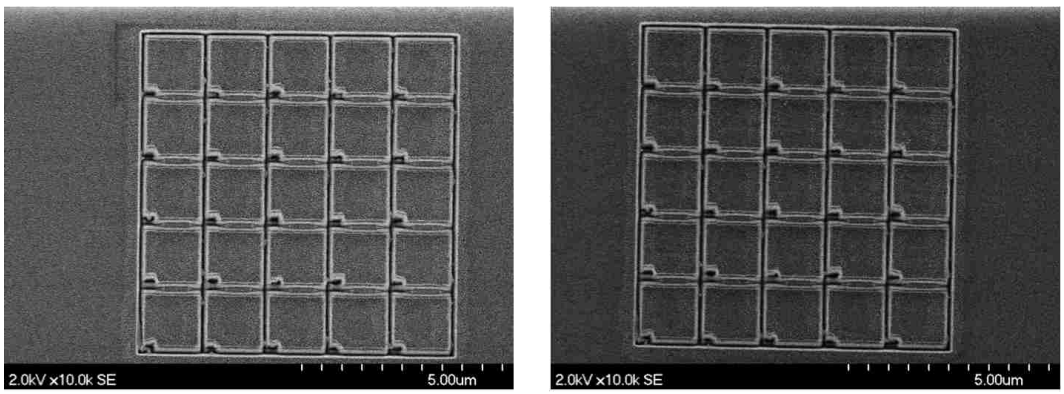

Figure 3.5: The entire FIB grid before and after ageing. The FIB grid can be found after ageing at $900\,^{\circ}\mathrm{C}$ and the orientation can be the same to allow for easy comparison of the same spot for analysis.

which lead to some irregularities, which will be addressed in later sections, in the results. So a new method of creating nanoparticles had to be developed. Instead of doing the VTZ, the 1.5 nm thin film of Pd on the single crystal was reduced in 3% hydrogen with the balance of nitrogen for 60 minutes at a temperature of $450\,^{\circ}\mathrm{C}$ with a ramp rate of $5\,^{\circ}\mathrm{C}$ per minute. Particles created from both methods produce similar sized particles, Figure 3.6, of about 15 nm in diameter on the YSZ substrate.

Then the samples with the nanoparticles are aged in a tube furnace with flowing gas over the samples. The samples are aged at either $900\,^{\circ}\mathrm{C}$ in N_2 that has been passed through an oxygen trap or at $700\,^{\circ}\mathrm{C}$ in 3% H_2 with the balance of N_2. The duration of these ageing experiments are in 12 hour increments.

After the ageing of the samples, the samples are imaged with the SEM and analyzed in the same way as the vacuum experiments. Using the PGT Spirit software to obtain the same information from the images, including the particle diameter.

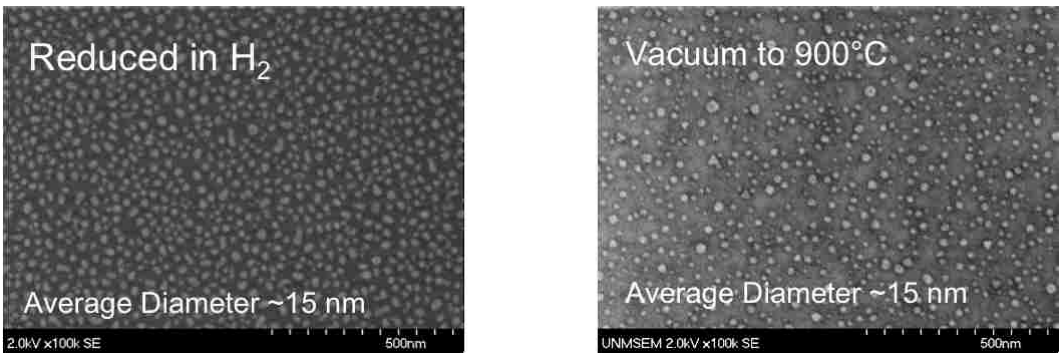

Figure 3.6: Comparing the two methods to produce nanoparticles on the substrate, the reduction of a Pd thin film (left) and the process of heating the sample in vacuum to $900\,^{\circ}\mathrm{C}$ (VTZ) (right).

3.2 Theoretical

Two different techniques were used to help analyze the experimental results. Results directly from the experiments are tested by deterministic models and by atomistic Monte Carlo Simulations.

3.2.1 Deterministic Models

The first of the two different deterministic models used is for the evaporation which is occurring directly from the metal nanoparticle. The second deterministic model that will be used is a sintering model based on Ostwald ripening while assuming that the attachment/detachment of adatoms is the rate limiting step.

Theory of Direct Evaporation from a Nanoparticle

In 1913, Langmuir [13] published the fundamental results of relating evaporation of a metallic film to the vapor pressure of the metal:

$$m = \sqrt{\frac{M}{2\pi RT}} p \tag{3.1}$$

where m is the rate of evaporation of the metallic film, with units of mass per time per unit area , M is the molecular weight of the metal, R is the gas constant, T is the absolute temperature, and p is the vapor pressure of the metal. However, to apply this to particles with curvature, the Gibbs-Thomson equation must be used:

$$\frac{dR_p}{dt} = \frac{m}{\rho} \exp\left(\frac{2\gamma\Omega}{R_p kT}\right) \tag{3.2}$$

where R_p is the particle radii, ρ is the density of the metal, γ is the surface free energy of the metal, that we will assume to be constant, which Campbell has shown for very small particles γ is not constant [27], Ω is the atomic volume, k is the Boltzmann constant. For our system, Pd heated at $900\,^{\circ}\mathrm{C}$, the pre-exponential is 9.28×10^{-4} nm/s while the value in the exponential, which we will refer to it as the critical radius, is 2.72 nm, making eq. (3.2):

$$\frac{dR_p}{dt} = 9.28 \times 10^{-4}\ \frac{nm}{s} \exp\left(\frac{2.72\ nm}{R_p}\right) \tag{3.3}$$

Using eq. (3.3) on an experimental initial distribution of particles by programming a deterministic model in FORTRAN allowed for this equation to be applied to every particle that was imaged by the SEM and was selected to be analyzed. In this deterministic model, we took a very short time step, 0.001 seconds, to ensure greater accuracy. In our system, over 2200 particles were calculated from six SEM images and then normalized by the entire area of all of six images used for the entire collection.

From the results from the calculation, the mass of the system was found by applying eq. (3.3) to individual images taken with the SEM. From the radius of the particles, from either experimental or modeling approaches, and assuming spherical particles, the entire mass of the image could be calculated by the summation of each individual nanoparticle via:

$$mass = \sum_{i=0}^{n} \frac{4}{3}\pi\rho(R_{p_i})^3 \tag{3.4}$$

Theory of Ostwald Ripening Sintering

The kinetic equations and assumptions for Ostwald ripening are described in this section in order to better understand how the deterministic model was developed and applied. The following is a summarized version from Wynblatt and Gjostein [7] and from Campbell and Parker [28]. The first assumption is the that each metal particle, is assumed to be spherical in shape with some contact angle, θ. The volume of a particle is:

$$V = \frac{4}{3}\pi R^3 \alpha_1 \tag{3.5}$$

where α_1 is defined as:

$$\alpha_1 = \frac{2 - 3cos(\theta) + cos^3(\theta)}{4} \tag{3.6}$$

It is assumed that the particle-size probability distribution, based of f(R,t), is continuous,

$$\frac{\partial f}{\partial t} = -\frac{\partial}{\partial R}\left(f\frac{dR}{dt}\right) \tag{3.7}$$

and that the volume of the system is constant:

$$\frac{4}{3}\pi\alpha_1 \int_0^\infty fR^3\, dR = \text{constant} \tag{3.8}$$

Two different rates are significant to the ripening of particles. The net rate that adatoms leave the surface to attach to the particle (J_p),

$$J_p = 2\pi R sin(\theta) a\beta'(c_s^{'} - c_p\beta) = X(c_s^{'} - c_p\beta) \tag{3.9}$$

with

$$X = 2\pi R sin(\theta) a\beta' \tag{3.10}$$

and the net rate of diffusion of adatoms on the surface to the particle (J_s)

$$J_s = \frac{2\pi D_1}{ln[(L/R)sin(\theta)]}(\bar{c}_s - c_s^{'}) = Y(\bar{c}_s - c_s^{'}) \tag{3.11}$$

with

$$Y = \frac{2\pi D_1}{ln[(L/R)sin(\theta)]} \tag{3.12}$$

It is also assumed that there is a concentration gradient near the particle/surface interface, this is because there is an energy well of adatoms at the surface of the particle, because the adatoms bind much more strongly to the particle than the substrate, more adatoms are at the particle/surface interface. The concentration of adatoms on the surface next to the edge of the particle is denoted by $c_s^{'}$. The concentration of adatoms far from the particle will be noted as $\bar{c}_s$. For an adatom to leave the particle, it must become a "monomer on the particle". The concentration of monomers on a particle is noted as c_p.

If the assumption is made that the adatom concentration directly adjacent to a particle is at steady state, then derivative of $c_s^{'}$ with respect with time is approximately 0, then the two fluxes, J_p and J_s, can be equated and then the concentration of adatoms next to the particle, $c_s^{'}$, can be solved for. This gives:

$$J_p = \frac{XY}{X+Y}(\bar{c}_s - c_p\beta) \tag{3.13}$$

The concentration of monomers on a particle, c_p, can be expressed as the equilibrium concentration of adatoms on an infinitely large particle, ${c_p}^{eq}$, the term $\bar{c}_s$, the concentration of adatoms far from the particle can be expressed as concentration of adatoms on the surface in equilibrium with an infinitely large particle, ${\bar{c}_s}^{eq}$.

Since the particles have curvature, the Gibbs-Thomson (GT) relation will be used. We can use the GT relation to express the equilibrium concentration of adatom species with the surface and with a particle. This gives us a relationship dependent on the radius of the particle. If we use this relationship and substitute it back into the flux term, eq.(3.13), and simplify, it gives:

$$J_p = \frac{XY}{X+Y}\beta c_p^{eq}\left(exp\left[\frac{2\gamma_m\Omega}{kTR^*}\right] - exp\left[\frac{2\gamma_m\Omega}{kTR}\right]\right) \tag{3.14}$$

There are two different rate limiting regimes. The attachment/detachment of adatom limiting case, where Y <<X,

$$J_p = Y\beta c_p^{eq}\left(exp\left[\frac{2\gamma_m\Omega}{kTR^*}\right] - exp\left[\frac{2\gamma_m\Omega}{kTR}\right]\right) \tag{3.15}$$

and the diffusion limiting case, where X<<Y,

$$J_p = X\beta c_p^{eq}\left(exp\left[\frac{2\gamma_m\Omega}{kTR^*}\right] - exp\left[\frac{2\gamma_m\Omega}{kTR}\right]\right) \tag{3.16}$$

To solve for the change in radius over time, the assumption that the volume is constant in the system is now used, eq. (3.5), into the particle-size probability distribution equation, eq. (3.7), to get an expression in terms of change in radius per time in terms of our flux of adatoms:

$$\frac{dV}{dt} = \frac{d}{dt}\left(\frac{4}{3}\pi R^3\alpha_1\right) = 4\pi R^2\alpha_1\left(\frac{dR}{dT}\right) = J_p\Omega \tag{3.17}$$

When the derivative is solved for, for each limiting case the final equation is for each of the limiting case: for the attachment/detachment limiting case is:

$$\frac{dR}{dt} = \frac{sin(\theta)\alpha\beta^{'}\beta c_p^{eq}\Omega}{2\alpha_1 R}\left(exp\left[\frac{2\gamma_m\Omega}{kTR^*}\right] - exp\left[\frac{2\gamma_m\Omega}{kTR}\right]\right) \tag{3.18}$$

and for the diffusion limited case:

$$\frac{dR}{dt} = \frac{D_1\beta c_p^{eq}\Omega}{2ln[(L/R)sin(\theta)]\alpha_1 r^2}\left(exp\left[\frac{2\gamma_m\Omega}{kTR^*}\right] - exp\left[\frac{2\gamma_m\Omega}{kTR}\right]\right) \tag{3.19}$$

Then eq. (3.18), for the attachment/detachment case is assumed to be the rate limiting case. Then much like for the direct evaporation, every particle in the system has eq. (3.18) applied to it in a Fortran program and the program is run for a certain specified time duration. The results from this model are then compared to experimental results. Mass is calculated the same way as in the evaporative model, by eq. (3.4) and the particle size distributions are used directly from the output files.

3.2.2 Atomistic Monte Carlo Simulations

The atomistic Monte Carlo Simulations (aMCS) were used to help better understand the experimental systems. In order to get the mircographs from the SEM into a format that would be compatible with the simulation software many steps had to be carefully done. The first few steps are similar to the analysis of the SEM micrographs, the images are imported into ImageJ where they are cropped, cleaned up and turned into a binary image. The binary image is then converted into a text file, where one numerical value is assigned to the dark pixels and another numerical value is assigned to the the light pixels.

Then depending on the size of the image and how large the particles are, the image can be divided into multiple files for analysis so the simulation does not take an excessive amount of time. After the image is an appropriate size for the simulation, a program is run

on the file to assign a correct calibration for how many atoms is in each pixel, typically for an SEM image at 300,000X magnification and for a metallic particle it is 1 pixel for 1 atom and for a 100,000X magnification image, it is 1 pixel for a 3x3 set of atoms. It also gives the particle a three dimensional shape, based on how large the cluster is and the height is half the diameter. As seen in Figure 3.7, the final product from the Monte Carlo simulation is very much like the original SEM image.

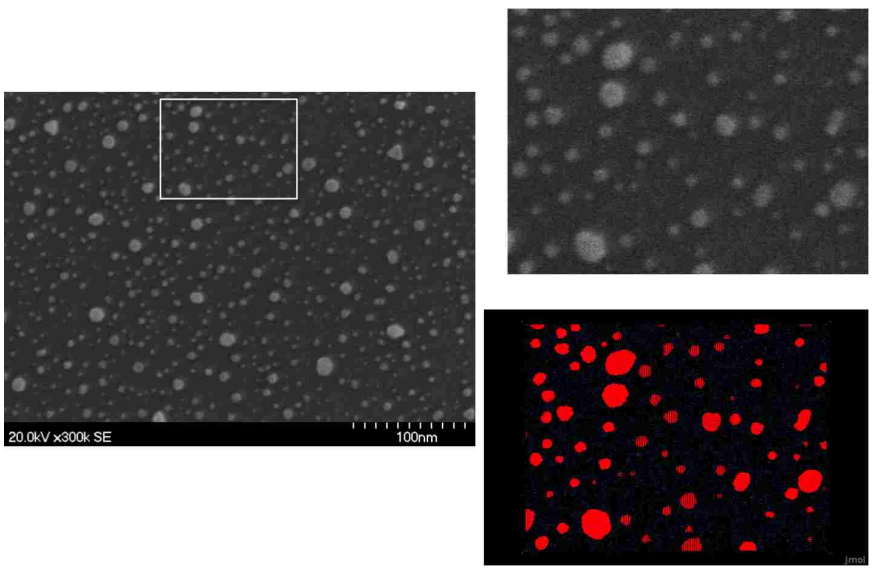

Figure 3.7: The entire SEM image, left, was cut into nine pieces for the aMCS, the images on the right show one of the nine sections, highlighted by the box, the top, is of the SEM image and the bottom is the file from the aMCS, the two are very similar.

The output from this file is run with a different program which will assign the gaseous atmosphere, for vacuum, there are no atoms in the gaseous phase and for the sintering experiments an inert gas of a density of 0.001. The output file for this program is then used as the input file for the aMCS. Also, a configuration file is needed for the running of the simulation, this file contains the binding energies of the metal to metal, the metal to substrate, and the metal to the ceiling.

Evaporation Environment

For the evaporation simulation, the metal atoms have a very large attraction to the ceiling, Figure 3.8. Once an atom is emitted from a particle, the atom will be attracted to the ceiling greater than the substrate or the metal particle. This will cause the atoms to travel a step at a time towards the ceiling through the atmosphere and once an atom reaches the ceiling, the probability for it to leave will be low. In experiments, once an atom leaves the particle, it will behave in a ballistic motion away from the sample, leaving no probability of the atom coming back towards the particle but this simulation can approximate how the system would thermodynamically operate by a step by step process. This simulation can capture atoms that do migrate on the surface.

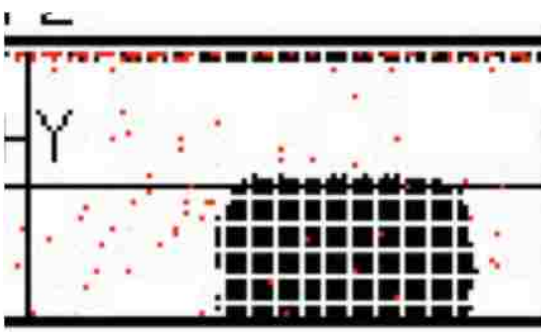

Figure 3.8: Cross sectional image of the aMCS process of evaporation, the very attractive ceiling is on top with many atoms already captured by it with more atoms approaching the ceiling. Also, atoms can be seen on the substrate. Image courtesy of Sivakumar Challa

Sintering Environment

For the sintering simulation, the simulation environment is at an elevated temperature, where sintering will occur. There are enough inert gas atoms in the simulation environment that there is a probability that the adatoms emitted to the atmosphere will collide with the gas atoms and be redirected, similar to what is believed to happen in a real inert

gas atmosphere where sintering happens experimentally. Much like the evaporation simulations, the system is allowed to evolve over time and periodically there are snapshots during the simulation to see how the system is evolving.

In the sintering experiments two different types of surfaces were looked at. A wetting surface, where the metal atoms are more strongly attracted or bound to the substrate, and a non-wetting surface, where the metal atoms are not as strongly attracted or bound to the substrate, as depicted in Figure 3.9. These simulations demonstrate how the metal/surface interfacial energies may play a role in catalyst sintering. Wether or not a strong metal/support interaction will help or hinder resistance to sintering.

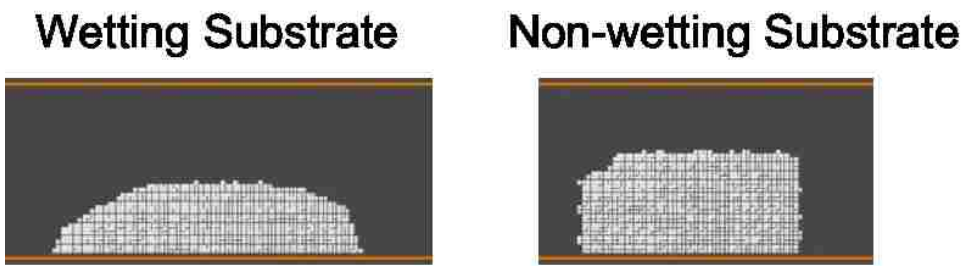

Figure 3.9: Cross sectional image of the aMCS process of sintering, on the left, is a wetting substrate, where the metal atoms are strongly attracted to the substrate, on the right, is a non-wetting substrate, where the metal atoms are not as attracted to the substrate. Image courtesy of Sivakumar Challa

Chapter 4

Evaporation of Nanoparticles from Model Surfaces

These evaporation experiments were performed under high vacuum conditions to measure the emission or evaporation rates of palladium nanoparticles on different substrates. These results are first looked at macroscopically to see the trends of of thousands of particles that were examined. In later sections, these results will be compared to microscopic studies of evaporation along with sintering studies under inert atmospheres.

4.1 Evaporation of Pd adatoms on YSZ Model Surface

The initial particle size distribution for Pd on yttria stabilized zirconia (YSZ) obtained by the SEM gave rise to a particle size distribution with an average particle size of 13.9 nm and a calculated mass, from eq. (3.4), of 2.4×10^{-14} g/μm^2. As the samples were aged in vacuum at $900\,^{\circ}\mathrm{C}$ for 30 minute increments, the mass steadily decreased, to values of 1.1×10^{-14} g/μm^2 for 30 minutes of ageing and 0.4×10^{-14} g/μm^2 for 1 hour of ageing, with virtually no detectable Pd observed on the surface after 1.5 hour of vacuum ageing.

Figure 4.1 displays the SEM images and shows that even though the mass is decreasing in each image, the average diameter is fairly constant, starting at 13.9 nm $\pm$ 0.25 nm, after 30 minutes it is 17 nm $\pm$ 0.4 nm, and after 1 hour of ageing the average diameter is 14.1 nm $\pm$ 0.25 nm, the error is the standard deviation of the mean of all images analyzed.

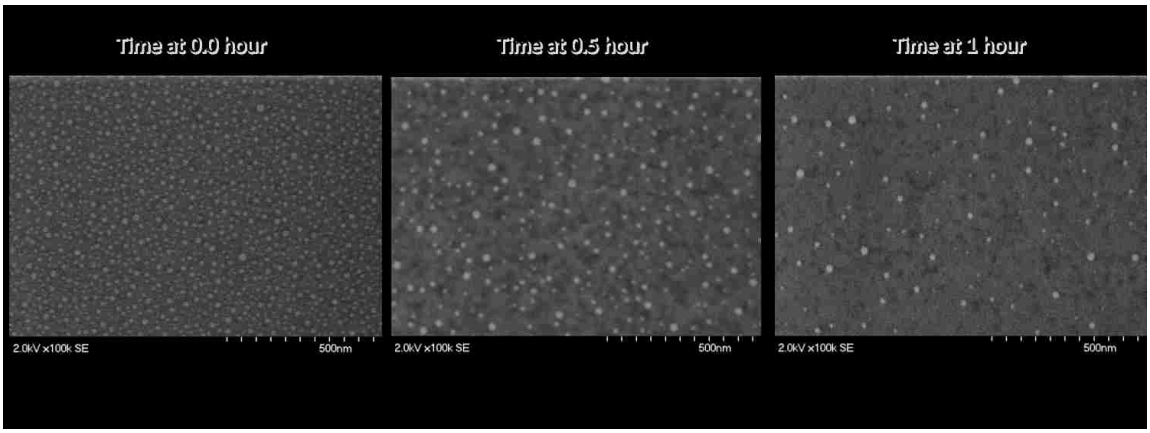

Figure 4.1: High Resolution Scanning Electron Micrographs of Pd on YSZ, images taken after half hour increments of ageing in high vacuum at $900\,^{\circ}\mathrm{C}$

The particle size distribution of the three ageing times, in Figure 4.1, are displayed in Figure 4.2. The particle size distributions are normalized per square micron. The particle size distribution maintained the overall shape over the times aged only loosing particle density per square micron. However, after the 30 minutes of ageing, there is a slight increase in larger particles compared to the initial distribution.

When applying the deterministic model of direct evaporation, eq. (3.3), to the entire collection of nanoparticles from the initial sample, so that the particles could be $aged$ over a range of 100 minutes in vacuum at $900\,^{\circ}\mathrm{C}$ in order to observe how evaporation would occur if the only mechanism of evaporation was direct evaporation from a nanoparticle. The plotting of the particle size distribution, Figure 4.3 of five different times over a 100 minute interval was done to visualize how the particle size distribution and mean diameter would evolve during direct evaporation ageing. This particle size distribution lost small

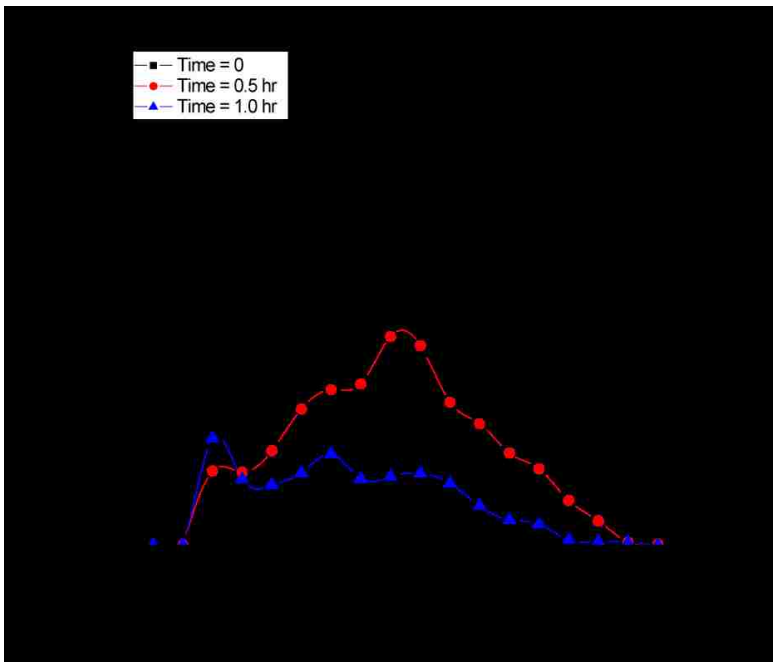

Figure 4.2: Experimental Particle Size Distributions for Pd on YSZ obtained from SEM images after ageing in high vacuum at $900\,^{\circ}\mathrm{C}$

particles rapidly, while loosing larger particles more slowly, the particle size distribution shifted down in particles per square micron while the peak of the distribution and the mean, table 4.1, shifted slowly towards smaller particles.

Direct Evaporation Model Mean	
Time	Average Diameter
0 min	13.9 nm
10 min	13.0 nm
30 min	11.4 nm
60 min	9.7 nm
80 min	8.5 nm
100 min	7.7 nm

Table 4.1: The Average Particle Diameter for the Distributions in Figure 4.3 based on the Gibbs-Thompson Equation for Evaporation

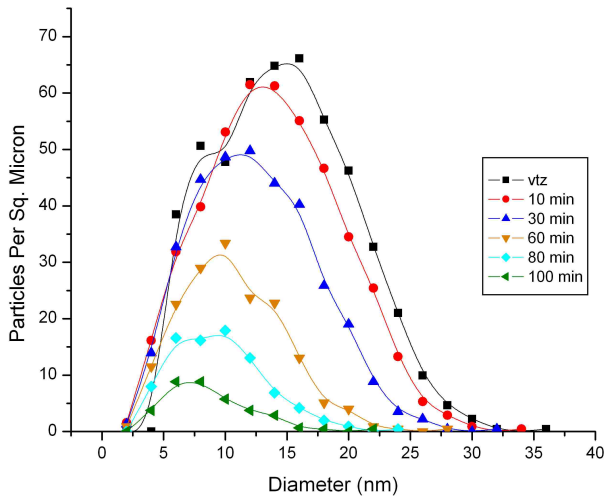

Figure 4.3: Predicted Particle Size Distribution Calculated from the Gibbs-Thompson Equation based on the initial experimental particle size distribution

As seen in the particle size distributions of both the experimental data and of the deterministic calculations, particles below 5 nm are not frequently in the sample. This is due to the conditions at which the experiments and calculations are performed, at $900\,^{\circ}\mathrm{C}$ and under high vacuum conditions. The vapor pressure of Pd at $900\,^{\circ}\mathrm{C}$ is 6.35 x 10^{-8} Torr and a critical radius of 2.72 nm, or diameter of 5.44 nm, meaning that particles with a radius below the critical radius are unstable and will evaporate quickly. This is demonstrated in Figure 4.4, showing a high resolution SEM image of the sample, showing that a 5 nm particle is visible on our microscope. The plot in Figure 4.4 also includes a plot of a particles lifetime according to eq. 3.3, the direct evaporation model of a nanoparticle, which shows that a 4 nm particle lifetime on the surface under the ageing conditions, is less than 200 seconds. Given that a very small particles lifetime on the surface is not very long, accounts for why there are so few of them present in the particle size distributions.

In comparison of the direct evaporation model, an atomistic Monte Carlo simulation

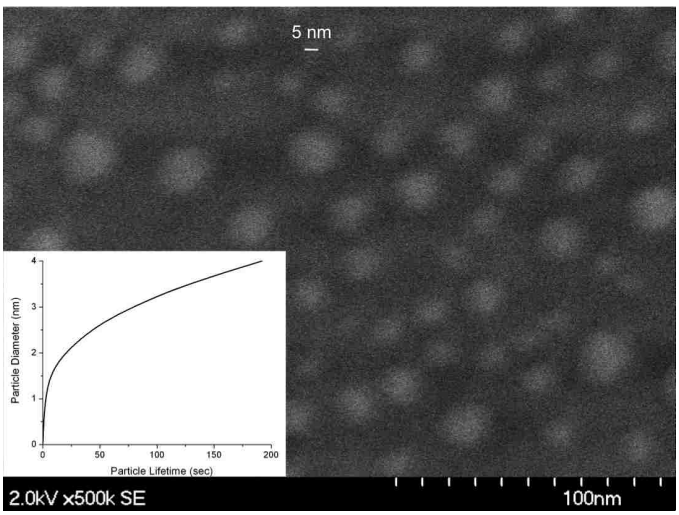

Figure 4.4: SEM image taken of Pd on YSZ at a high magnification to show the resolution of the microscope and to help identify the smallest features present on the sample, the inset plot shows the lifetime of a particle small nanoparticle under vacuum at $900\,^{\circ}\mathrm{C}$

(aMCS) was employed. While this step by step simulation does not entirely replicate the ballistic motion of the experimental vacuum ageing set up, it will provide us with insight into the overall trends of the most energy favorable evaporation trends. The aMCS will allow for both the emission of adatoms directly from the the particle into the vacuum-like atmosphere, but it will also allow for the diffusion of adatoms on the substrate. Using an initial size distribution of particles with similar sized particles and distribution to the Pd on YSZ, the Monte Carlo system was allowed to operate under a high temperature, vacuum like conditions for the observation of the evaporation of nanoparticles.

The evolution of the particle size distribution, Figure 4.5, taken at several Monte Carlo time step intervals. The distribution loses most of the small particles very rapidly to shift to a new mean particle size, but after this new mean diameter is established the particle size distribution decreases around this new mean and decreases in particles per area. These trends tell us how a system under evaporation like conditions will evaporate while allowing for both direct evaporation and surface mediated diffusion.

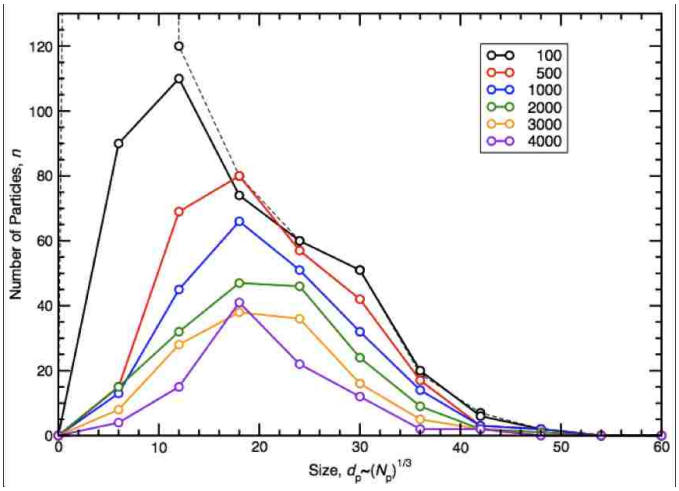

Figure 4.5: Particle Size Distribution of Pd nanoparticles from Atomistic Monte Carlo Simulations, times are in Monte Carlo Steps

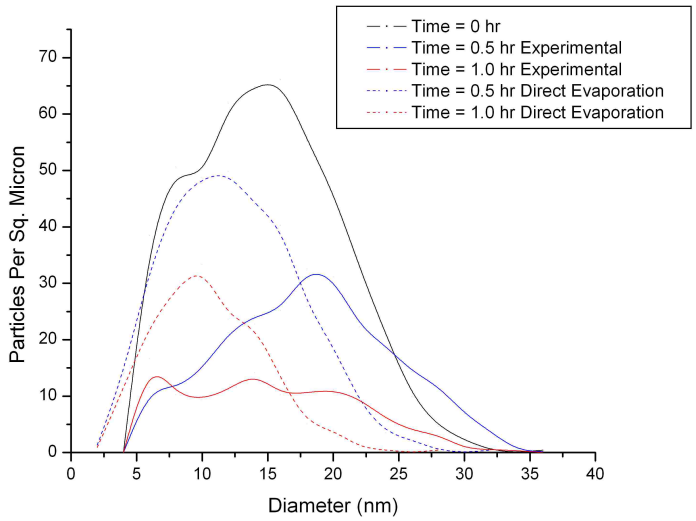

Figure 4.6: Comparing the Particle Size Distributions of experimental data (solid) and from the prediction for direct evaporation (dashed)

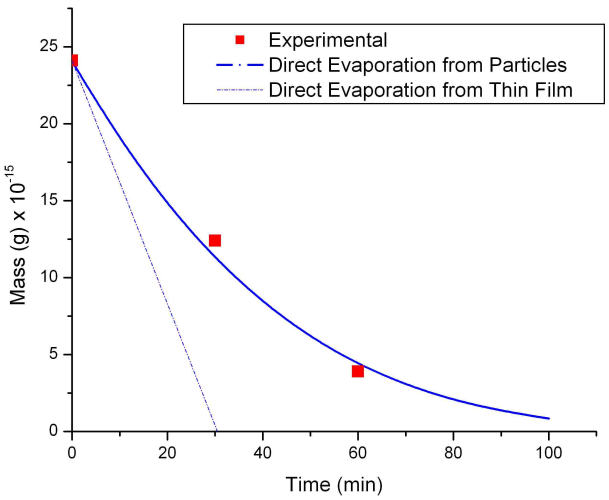

Figure 4.7: Comparing the rate of evaporation from the direct evaporation from nanoparticles (solid line) which agrees very well with experimental data (square points). For comparison we also show direct evaporation from a thin film having the same total mass (dashed line)

From comparing the direct evaporation particle size distribution and the experimental particle size distribution, see Figure 4.6, and noticing the trends from the aMCS that the particle size distribution shifts down, we can infer that particles are ripening to other particles during the evaporation process. From comparing the mass loss of the system, Figure 4.7, we can also see that the expected mass loss is the same as what to be expected if only direct evaporation was occurring and it is much less that what would be expected from a thin film evaporating.

Speculating a mechanism for evaporation based on the observations from the macroscopic study, we believe that there are adatoms being evaporated directly from the nanoparticle into the vacuum and that there are adatoms diffusing from the particle onto the substrate, as seen in Figure 4.8. If direct evaporation was the only mechanism occurring, then the particle size distribution would look like Figure 4.3 with all particles decreasing in size.

However, with the particle size distributions of the experimental results, Figure 4.2, with the particles maintaining their size and even increasing their size, leads us to believe that surface ripening is also occurring during evaporation. In the aMCS, which would allow for both types of evaporation, direct from the particle and from the surface, in Figure 4.5, the particles do not decrease in size, as observed in the direct evaporation model, but maintained their overall shape during evaporation, as observed in experimental results. These observations, this experimental evidence leads us to believe that the mechanism consists of direct evaporation along with surface diffusion contributing to the ripening of particles.

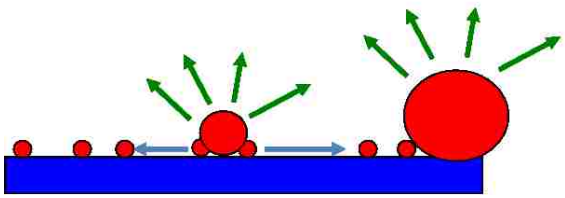

Figure 4.8: The proposed evaporation mechanism of Pd on YSZ under vacuum, there is direct evaporation from the nanoparticle, but there is also surface diffusion ripening from small particles to larger particles

4.2 Evaporation of Pd adatoms on Other Metal-Oxide Model Surfaces

In other evaporation experiments, other metal oxide substrates were used to understand the nature of the support on the emission of adatoms. alumina and quartz were both used as comparisons to YSZ to help understand the influence of the substrate on evaporation and how that may help understand why metal nanoparticles sinter differently on different supports.

Palladium supported on α-alumina after the initial VTZ treatment the particles have an

average size of around 15 nm and a mass of of 2.7×10^{-14} g/μm^2 from the SEM images, Figure 4.9. After ageing treatments at $900\,^{\circ}\mathrm{C}$ for half hour intervals, the mass decreased after half an hour to 1.3×10^{-14} g/μm^2 and after one hour of cumulative ageing the mass was 0.8×10^{-14} g/μm^2. During the evaporation experiments, the average diameter of system went from the initial size of 15.2 nm $\pm$ 0.8 nm, to 12.4 nm $\pm$ 0.3 nm after half an hour and 13.7 nm $\pm$ 0.4 nm after an additional half hour of vacuum ageing, the error is the standard deviation of the mean of multiple images taken at random sites on the single crystal wafer. Again, as with the Pd on YSZ sample, the mass steadily decreased in the vacuum but the mean particle size stayed relatively constant, between 12 and 15 nm.

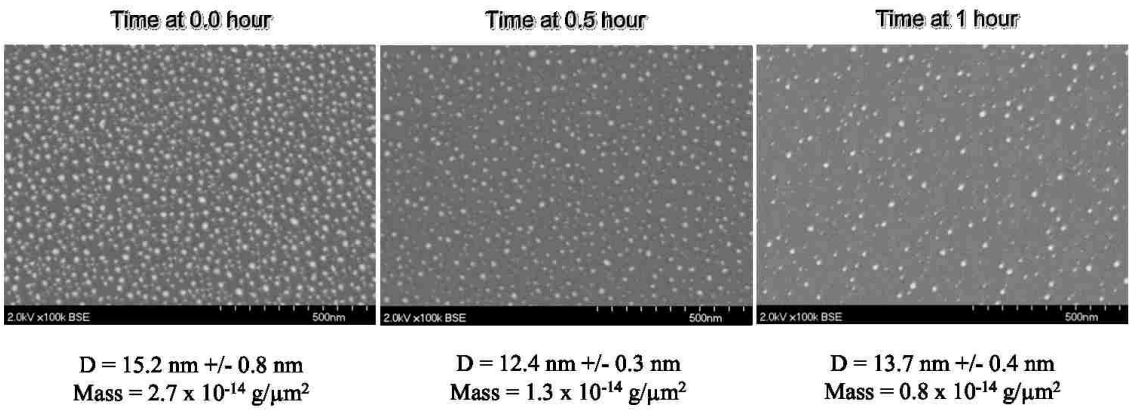

Figure 4.9: High Resolution Scanning Electron Micrographs of Pd on Al_2O_3, images taken after half hour increments of ageing in high vacuum at $900\,^{\circ}\mathrm{C}$

The particle size distribution of Pd on alumina, Figure 4.10, shows the same tendencies as the Pd on YSZ sample, with the distribution finding a new mean after the first half hour of ageing, then the particle size distribution simply shifts looses particles and the particle size distribution is simply sifted down. The number of large particles, between 23 and 30 nm in diameter, stays constant between half and hour and an hour of vacuum ageing. This would favor that the larger particles are somewhat stable at these elevated temperatures and that while the smaller particles are evaporating, that there is some ripening occurring

that is leading to the stability of the larger particles.

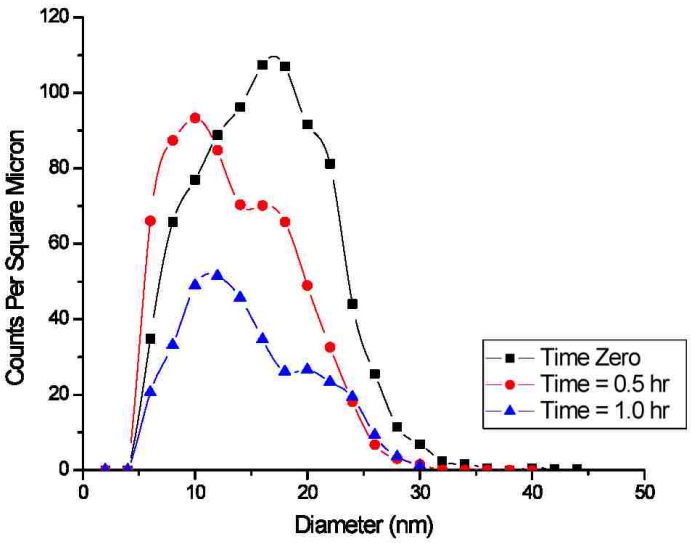

Figure 4.10: Experimental Particle Size Distributions for Pd on Al_2O_3 obtained from SEM images after ageing in high vacuum at $900\,^{\circ}\mathrm{C}$

The mass of the Pd on Al_2O_3 sample shows that the predicted evaporation rate exceeds that of what we see experimentally, Figure 4.11. The fact that more mass remains than would be be expected would suggest that other factors are contributing to the hindrance of Pd adatoms being emitted. This could be explained by work done by Tomsia's group at Lawrence Berkeley National Laboratories [29], in structural analysis studies by low-energy electron diffraction on the (0001) surface of α-alumina at around $1000\,^{\circ}\mathrm{C}$ under ultrahigh vacuum conditions, revealed that the alumina surface does undergo some reversible changes. This along with other work done by Tomsia's group showing that on alumina, that other metals, such as Ni, Pd, Pt, may form some type of alloy or strong bonding between the metal in the metal-oxide substrate. When the metal particle is at elevated temperatures, it exhibits liquid-like properties, this may allow for the metal-metal bond to form between the Pd and the Al in the Al_2O_3.

The present work, being performed at $900\,^{\circ}\mathrm{C}$, which was done very close to the temperatures that exhibited a reversible structural change to alumina, and with the work showing that the metals may bind with the metal in the metal-oxide, may help explain why the the Pd on alumina is not evaporating as we would expect. That some chemical bond may be created due to some reconstruction to the alumina and a bond is being formed that will not allow the Pd to evaporate as easily as expected.

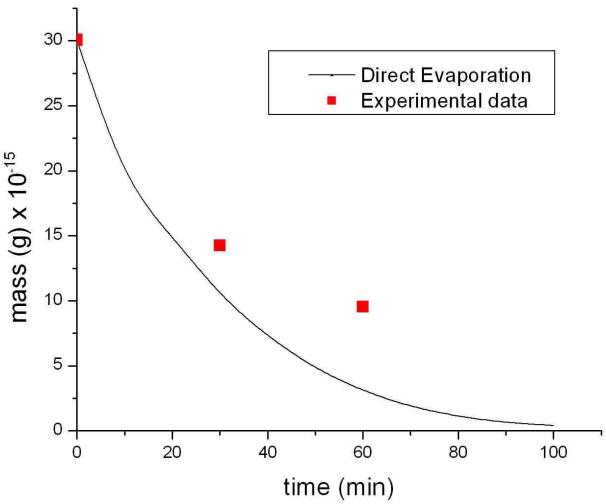

Figure 4.11: Comparing the rate of evaporation from the direct evaporation from nanoparticles (solid line) which is less than the experimental data (square points), meaning that evaporation is occurring slower than direct evaporation would predict

The other support looked at was Pd on quartz. After the initial VTZ treatment, Figure 4.12, the initial size was 9.9 nm $\pm$ 0.2 nm with a mass of 1.8×10^{-14} g/μm^2, much lower than the initial mass of both the Pd on alumina and Pd on YSZ supports. After half an hour of vacuum ageing, the mass decreased rapidly to 0.15×10^{-14} g/μm^2 and the diameter stayed around 10 nm to 10.4 nm $\pm$ 0.3 nm. After one hour of vacuum ageing, virtually all the Pd had evaporated from the surface as little Pd could be observed with the SEM.

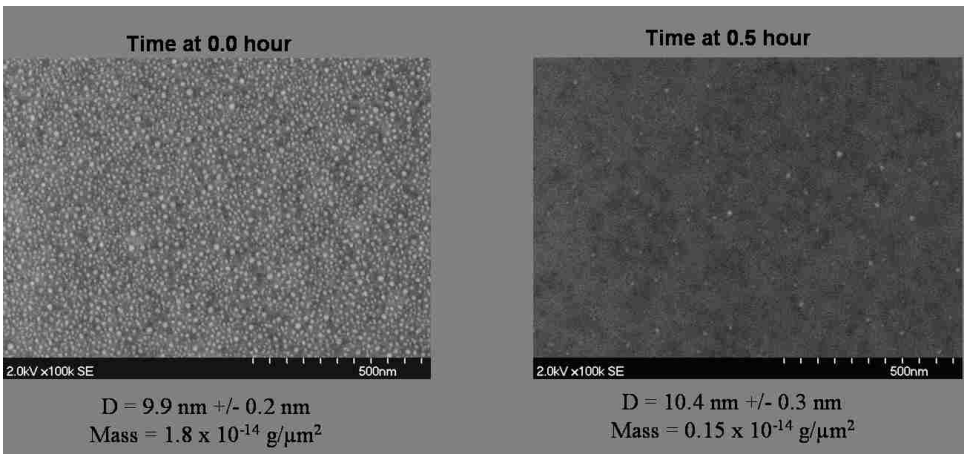

Figure 4.12: High Resolution Scanning Electron Micrographs of Pd on Quartz, images taken after half hour increments of ageing in high vacuum at $900\,^{\circ}\mathrm{C}$

The particle size distribution of the Pd on quartz, Figure 4.13 sample showed similar trends as the Pd on alumina and Pd on YSZ substrates, the initial particle size distribution decreased in particles per area around a common mean, of around 10 nm. Evaporation did occur much faster on quartz than the other substrates, after half an hour most of the Pd particles had evaporated, leaving virtually no Pd particles after 1 full hour of ageing under vacuum. The reason why quartz evaporated faster is not known, but it is speculated that Pd does not bind strongly towards the quartz surface, resulting in the evaporation of the Pd adatoms that are mobile on the substrate.

By comparing the calculated mass from the direct evaporation deterministic model, eq. (3.3) and comparing that to the mass calculated from the SEM images, Figure 4.14, the mass of the experiment is much less than that which is predicted from the deterministic model. Since there is more mass loss in the experimental results than would be expected, another mechanism other than just direct evaporation is contributing to the enhanced rate of which mass is lost.

The mechanism of Pd adatoms evaporating from quartz is most likely from adatoms

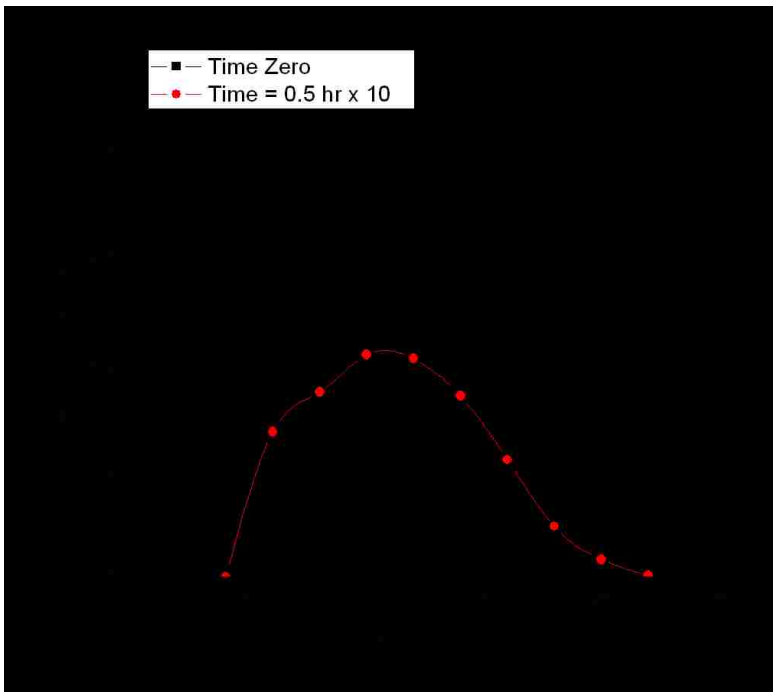

Figure 4.13: Experimental Particle Size Distributions for Pd on quartz obtained from SEM images after ageing in high vacuum at $900\,^{\circ}\mathrm{C}$, the plot after 0.5 hr of vacuum ageing has been multiplied by 10 to the the particles per square micron on the same y-axis as the initial plot in order to compare distributions

evaporating directly from the nanoparticles, via direct evaporation, and also from evaporation from the substrate as the adatoms are diffusing along the surface that are not strongly bound to the SiO_2 surface, Figure 4.15.

To gain a better understand of how evaporation occurs from nanoparticles, a microscopic approach was developed to complete the understanding of this macroscopic view of evaporation.

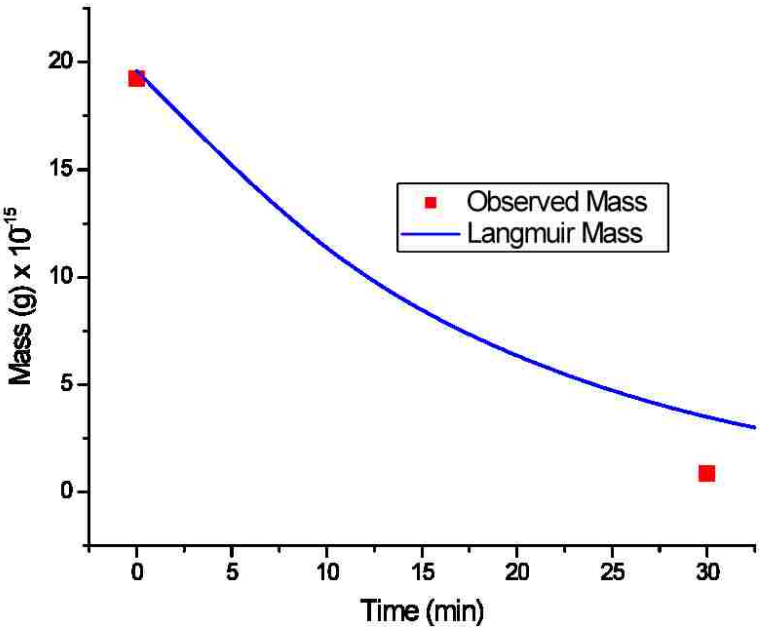

Figure 4.14: Comparing the rate of evaporation from the direct evaporation from nanoparticles (solid line) which exceeds the experimental data (square points), meaning that evaporation is occurring faster than just direct evaporation

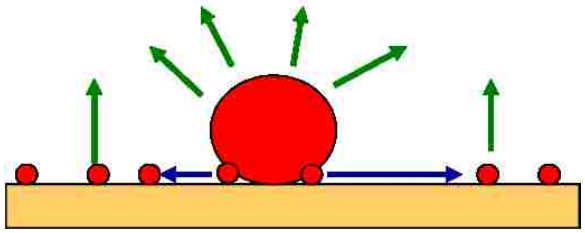

Figure 4.15: The proposed evaporation mechanism of Pd on quartz under vacuum, there is direct evaporation from the nanoparticle and additional evaporation from the diffusion of adatoms from the surface

Chapter 5

Microscopic Studies of Evaporation of Nanoparticles

Utilizing the markings created by the FIB, we could easily follow how individual particles evaporated. For the YSZ sample, the region inside the FIB region appeared to resemble the regions far from the FIB region, Figure 5.1. The average diameter of the image inside of the FIBed region is slightly smaller at 14.0 nm compared to the region from random areas far from the FIBed region, which were 16.0 nm. Also, from Figure 5.1, it is apparent that some of the particles near the edge of the of the FIBed region are not very rounded and very *jagged* in appearance, this is believed to be from some type of alloying from the gallium (Ga) deposits from the FIB etching, the Ga may have been in the single crystal of YSZ, then migrated out of the single crystal and alloyed with the Pd nanoparticles as they were formed.

With the FIB grid, regions inside the grid could be followed easily before and after ageing, Figure 5.2. Images taken at the same magnification of the same region can be observed before and after vacuum ageing. It is more clearly seen in a binary image, Figure 5.3, where the two images are overlapped. The binary image is composed of the initial

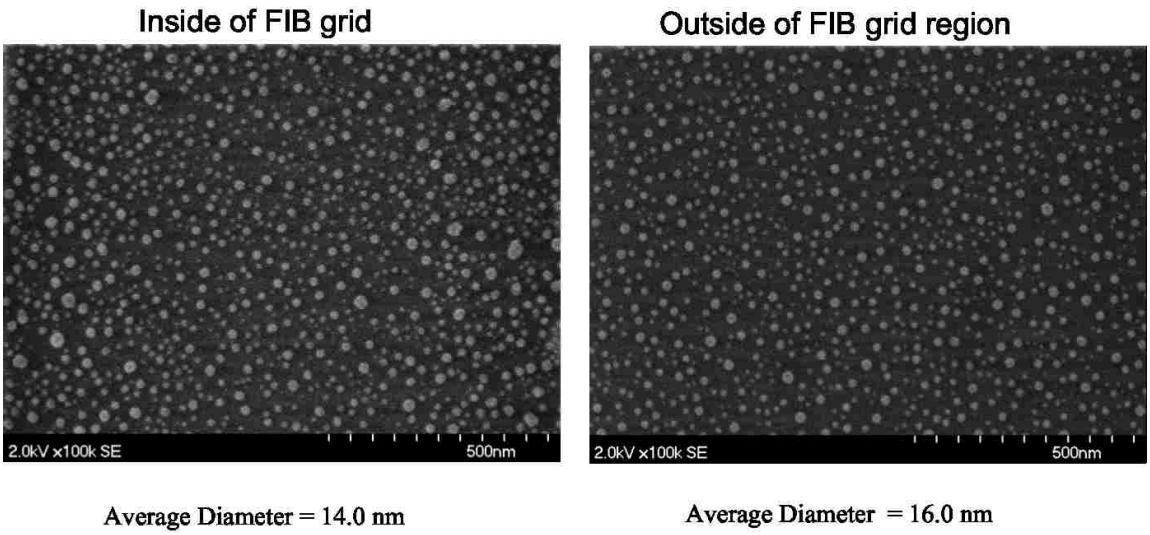

Figure 5.1: Comparing the regions on the YSZ wafer inside of the FIB grid, left, and the regions far from the FIB grid, right. The regions are similar in that they have similar average diameters but the region around the FIB etching, to the sides of the image on the left, the particles are very *jagged*.

VTZ image, highlighted in red and the aged sample, highlighted in blue. This overlapping binary image shows what particles evaporated and what particles remain after ageing, with the brighter particles are the particles remaining. The particles near the edge, towards the FIB grid markings, have a higher resistance to evaporation than the particles near the center, where the Ga beam may not have spent as much time during the etching. This resistance to evaporation is most likely due from a formation of a PdGa alloy.

A closer examination of the region inside of the FIB grid, Figure 5.4, and at a much higher magnification and following the same particles before and after ageing in vacuum. When applying the deterministic evaporation model, eq. (3.3), to these particles then tracking how the particles evaporated experimentally, we can compare how the particles evaporated in experiments to show how these particles would evaporate under a direct evaporation model. Select particles are labeled, in Figure 5.4, to how the evaporation

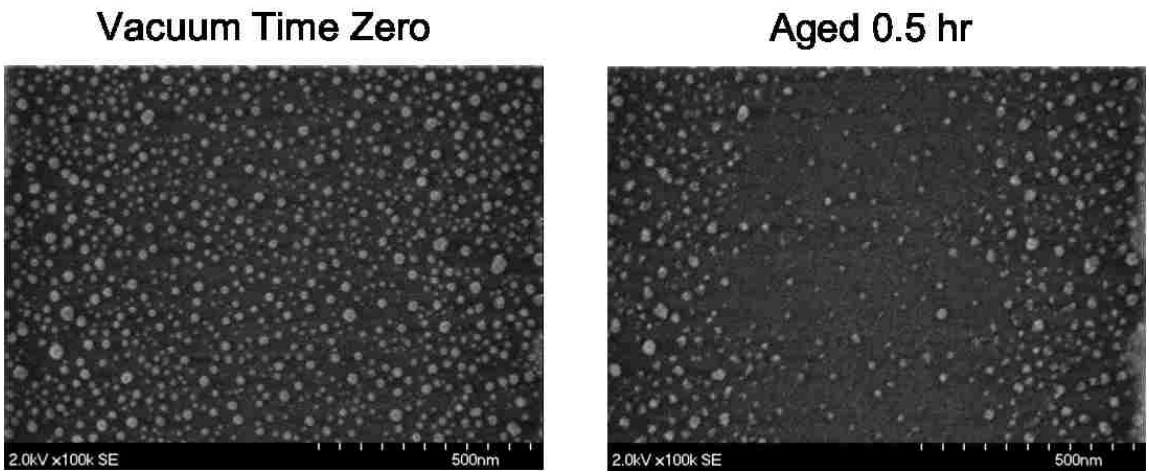

Figure 5.2: SEM images of the vacuum time zero, left, and after ageing in vacuum for 0.5 hr at $900\,^{\circ}\mathrm{C}$, right, showing the ease of looking at the same region before and after ageing.

experimentally compared to theoretical direct evaporation.

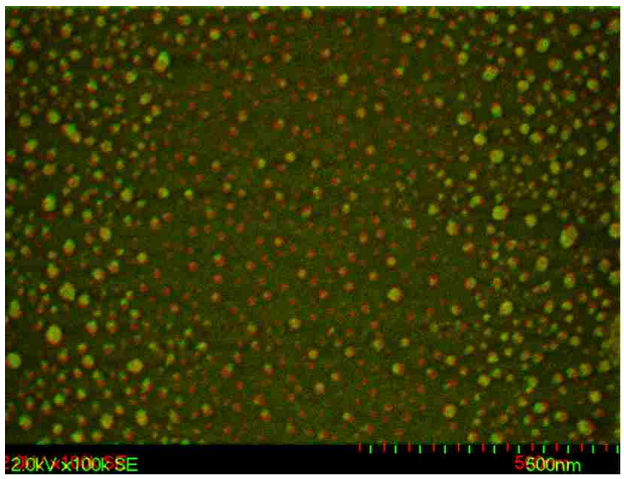

Figure 5.3: Binary image composed of the images from Figure 5.2, the VTZ image was shaded red while the aged image was shaded blue, giving the binary image. The particles that remained are much brighter than the darker particles that were originally on the sample, the particles nearest the gallium etching remained after vacuum ageing.

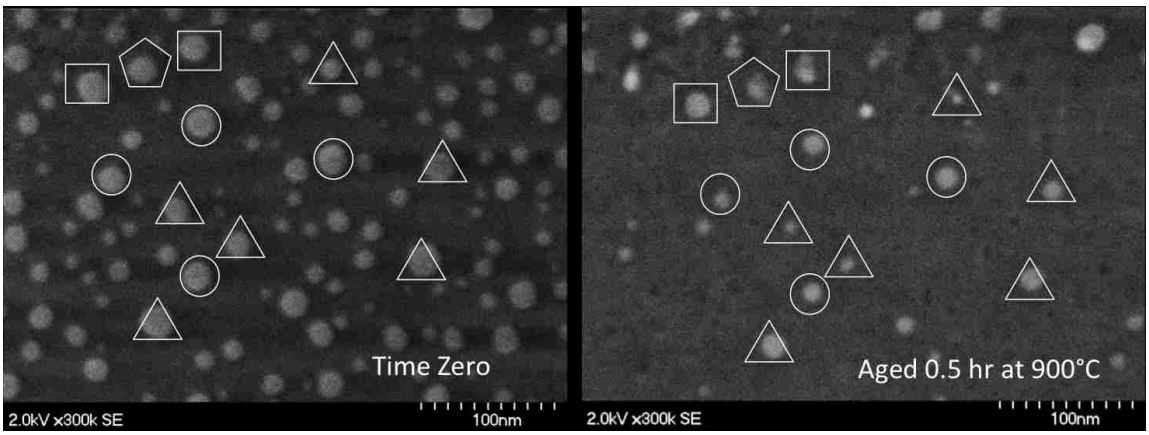

Figure 5.4: Using a patterned grid from a Focused Ion Beam, the same region can be viewed before and after ageing. The size of each particle is compared with the prediction for direct evaporation with squares indicating particles whose size agrees with the prediction, pentagons indicating particles whose sizes are greater than the prediction, while particles that are smaller by 5-15% are indicated by circles and those with sizes great than 15% smaller than predicted are indicated by triangles. Particles that have completely evaporated leave behind pits in the support

Also, the particle size distribution of the FIB region helps explain how the particles evaporate and interact with one another under the vacuum evaporation conditions, Figure 5.5. The particle size distribution, intentionally roughly binned to show how the peaks change over time. The smaller particles lose more after ageing while maintaining their mean size over the smaller particle size peak, while the larger peak's size does shift slightly over to even larger particles.

Other images within the FIB grid shows similar results to what was seen in the macroscopic view, that particles do grow under vacuum. Comparing the initial sample to that of the aged in vacuum image of a similar region, Figure 5.6, shows an individual particle that grows under vacuum. The initial particle is 35.1 nm in diameter, after ageing in high vacuum for 30 min, the particle actually grows to a diameter of 36.4 nm. While this is not substantial growth, this is clear evidence that particles are indeed ripening via a surface diffusion mechanism while also evaporating. A binary image, Figure 5.7, shows that the

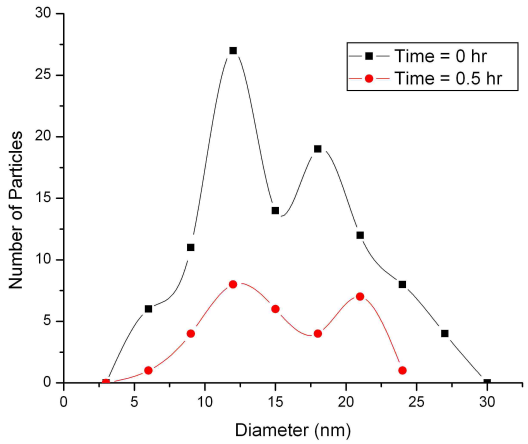

Figure 5.5: Particle Size Distribution from figure 5.4 where the same particles are examined before and after ageing. Average diameter is initially 14 nm and after ageing is 13.7 nm

aged particle, resulting in brighter particles when overlapped, shows that the particle measured is brighter without any fainter particle behind it, which is typical of particles that have evaporated and decreased in size.

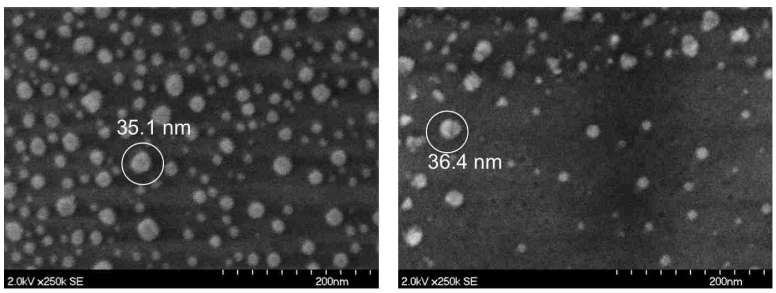

Figure 5.6: Viewing the same region before, left image, and after, right image, ageing in vacuum reveals that the particle circled grows from 35.1 nm to 36.4 nm after vacuum ageing at $900\,^{\circ}\mathrm{C}$

Having this microscopic view, it confirms what was seen experimentally in the macro-

Figure 5.7: Binary image of Figure 5.6 showing that the particle that grew after vacuum ageing has no faint halo around the particle, like most particles that have decreased in size from evaporation

scopic experiments. The observation of following individual particles and analyzing them showed that some particles did grow or lost less mass than expected under vacuum ageing conditions and that a number of the smaller particles lost much more mass than expected if direct evaporation was occurring, verifies the mechanism that was proposed, Figure 4.8, in the macroscopic observation that particles small particles ripened to larger particles via substrate diffusion of adatoms.

Also, a quartz wafer was etched with the FIB beam. Unfortunately , the Ga beam had adverse side effects to the single crystal of quartz. The sample within the FIB grid and far away from the FIB grid did not exhibit similar sizes or features, Figure 5.8. Inside of the FIB region the average diameter is 18.0 nm with many large nanoparticles and a few smaller nanoparticles along with some oddly shaped particles, for the regions far from the FIB grid, the average diameter was 12.1 nm with small, round particles scattered about the entire surface. It is thought that the Ga beam may have dwelled on the quartz surface

longer or due to the charging of the quartz, the beam hit more areas, causing more Ga to be deposited throughout the entire region of the FIB, not leaving a clean surface like the YSZ sample.

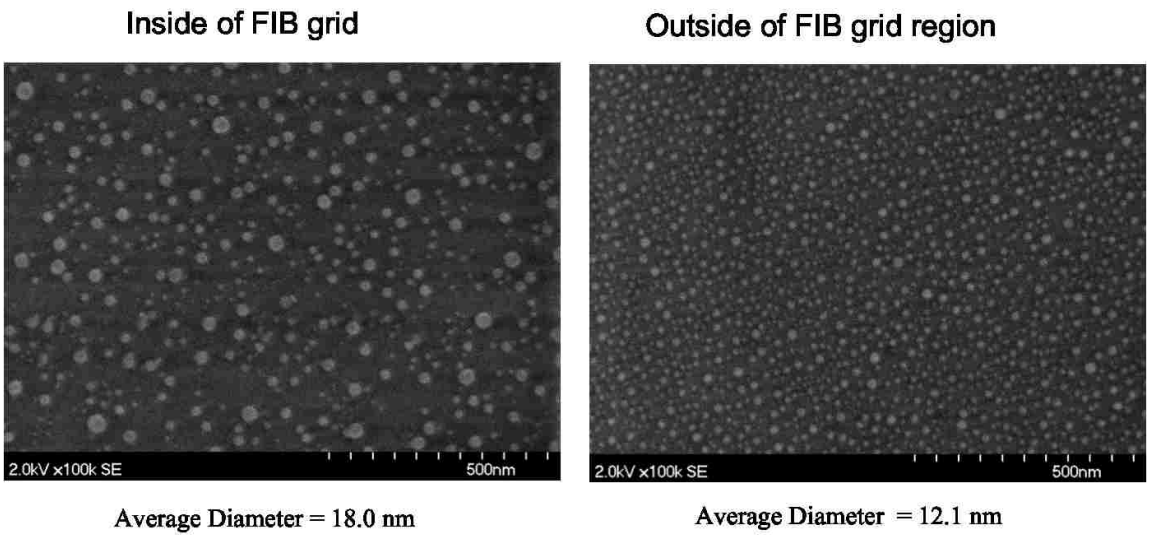

Figure 5.8: Comparing the regions on the quartz wafer inside of the FIB grid, left, and the regions far from the FIB grid, right. The regions are not similar, the region inside of the FIB region contains large particles with a few small particles scattered around, the region far from the FIB grid contains similar sized particles that are smaller than particles inside of the FIB grid.

Even though the surface inside the FIB region is not representative of the actual quartz sample, one interesting observation was observed. Before and after vacuum ageing treatments at $900\,^{\circ}\mathrm{C}$ for 15 min shows that a coalescence event may have taken place, Figure 5.9, giving evidence for particle migration, even under vacuum conditions. While it is not believed these events occur frequently and the possibility of the Ga on the surface may have helped the mobility of the Pd particles but this does allow for the possibility of particle migration and coalescence. It is not believed that the particles evaporated, since looking at the binary image in Figure 5.9 shows that particles of similar sizes in the same region did not evaporate significantly and are still present in the final image.

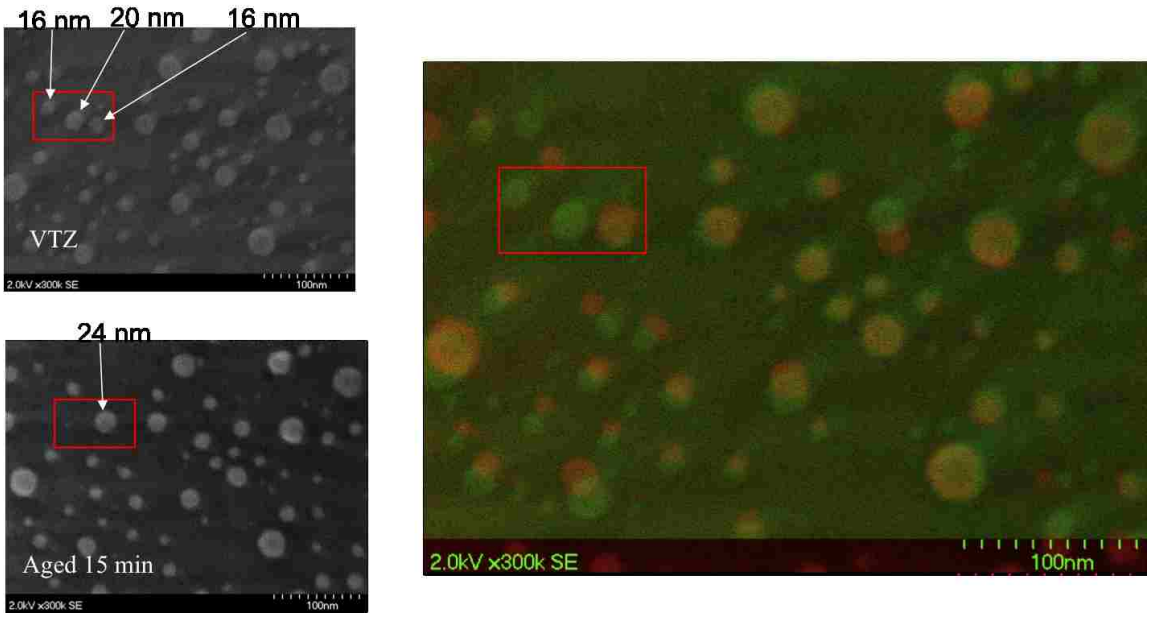

Figure 5.9: Observing Pd nanoparticles on a Quartz wafer that was modified with an etched grid, observing these particles three particles, labeled and enclosed in a red box, before vacuum ageing, top left, and then after vacuum ageing after 15 minutes, bottom left, reveals that these three particles seemed to have coalesced, note in the binary image, right, that particles of similar sized did not move or evaporate

Chapter 6

Sintering of Model Nanoparticle Systems

6.1 Sintering of Pd Nanoparticles at $900\,^{\circ}\mathrm{C}$

From the evaporation data, the support clearly plays a large role in rate of adatoms being emitted from the Pd nanoparticle. The next step in understanding how nanoparticles sinter, is to correlate the emission rates measured under vacuum to rates of sintering. If ripening is the main mode of sintering and under vacuum if the emission step of ripening could be captured by the vacuum and quantified, then sintering rates could be correlated against evaporation rates.

Sintering was performed under a nitrogen (N_2) atmosphere at $900\,^{\circ}\mathrm{C}$ for a duration of 12 hr. The three supports used in these experiments are the same as in the evaporation experiments performed at $900\,^{\circ}\mathrm{C}$; which are YSZ, quartz, and alumina. The first support discussed is Pd on YSZ.

Palladium on YSZ sintered the least of the three supports, Figure 6.1. The initial

VTZ sample had an average diameter of 10.6 nm, after 12 hours of ageing under N_2, the average diameter increased to 35.7 nm. The particle size distribution, Figure 6.2, shows an increase in larger particles also with a slight bimodel distribution. One peak after being aged for 12 hours is around a diameter of 20 nm while the other peak in the distribution is around 40 nm. There are clearly larger and smaller particles in the system as seen in the SEM image, Figure 6.1, and with a bimodel distribution after ageing, it has been proposed that a bimodel distribution could be because of ripening during the sintering conditions, while there is no evidence directly of ripening, the distribution may give us clues into the sintering mechanism. In a paper by Dellare, et. al. [30], it is proposed that a binary particle size distribution during the sintering of Pt on a porous alumina support in pure oxygen may be from ripening and possibly the migration of the nanoparticles, but under oxygen, an oxide forms on the smaller particles and causes the particles to split into smaller particles. While our sintering experiments were done in nitrogen, a small amount of oxygen may have been still been present and could have caused this phenomena to have occurred.

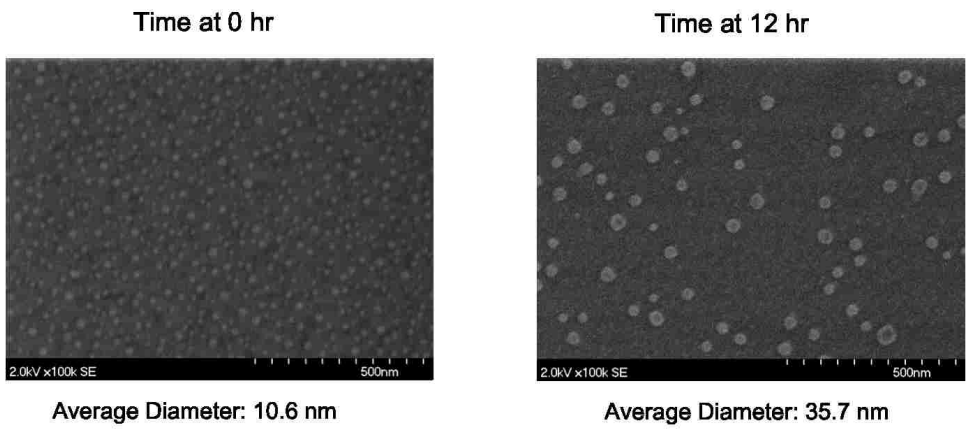

Figure 6.1: High Resolution Scanning Electron Micrographs of Pd on YSZ, initial image (left) and the image taken after 12 hours of ageing in nitrogen at $900\,^{\circ}\mathrm{C}$ (right)

Palladium on quartz sintered slightly more than the Pd on YSZ sample after 12 hours

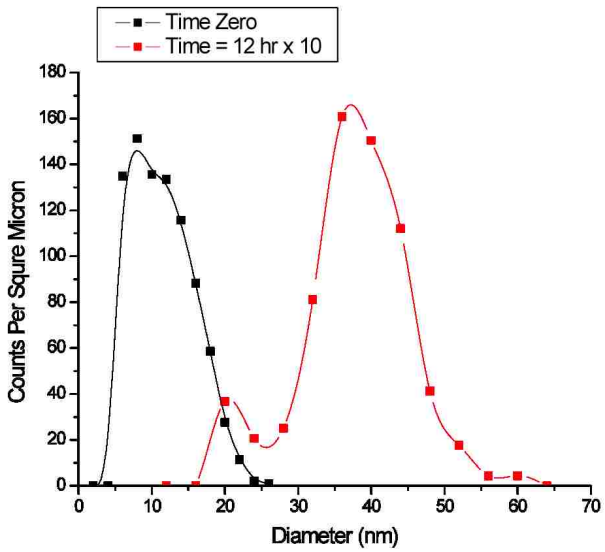

Figure 6.2: Particle size distribution plot of Pd on YSZ, plots are from before and after 12 hours of ageing in nitrogen at $900\,^{\circ}\mathrm{C}$, the aged sample is multiplied by 10 to get counts per square micron on the same axis to compare the distributions

of ageing in nitrogen. The sample had an initial VTZ average particle diameter of nearly 11 nm, but after 12 hours at $900\,^{\circ}\mathrm{C}$, the particles sintered to around 41 nm, as seen from the SEM images in Figure 6.3. The particles ranged from 15 nm to nearly 70 nm after the ageing, which was much larger than the Pd on YSZ sample that had the largest particle of around 60 nm. The particle size distribution, Figure 6.4, the initial distribution is Gaussian in shape, centered around 11 nm, then after 12 hours of ageing, the distribution is no longer Gaussian, but it is slightly irregular with a slight tail towards smaller particles.

Palladium on alumina sintered the most severe out of all three substrates, Figure 6.5. The particles were initially around 15 nm, but after 12 hours of ageing in nitrogen, the particles grew to over 65 nm in size, over 4 times the size of the initial particles. After ageing at $900\,^{\circ}\mathrm{C}$, the particle size distribution, Figure 6.6, developed a log normal type of distribution. A very large tail stretched from the center, of about 65 nm, to well over

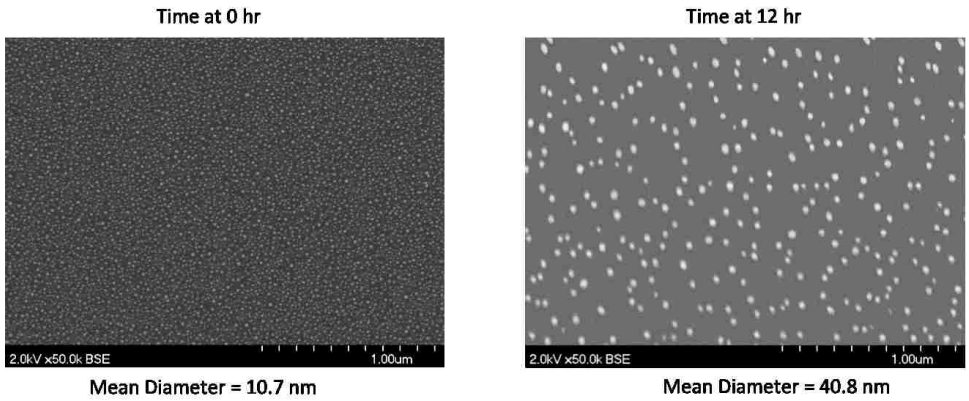

Figure 6.3: High Resolution BSE Scanning Electron Micrographs of Pd on quartz, initial image (left) and the image taken after 12 hours of ageing in nitrogen at 900 °C (right)

135 nm, over twice the mean. This type of distribution is associated with coalescence type sintering, not ripening. At such high temperatures and with small initial particle size, of

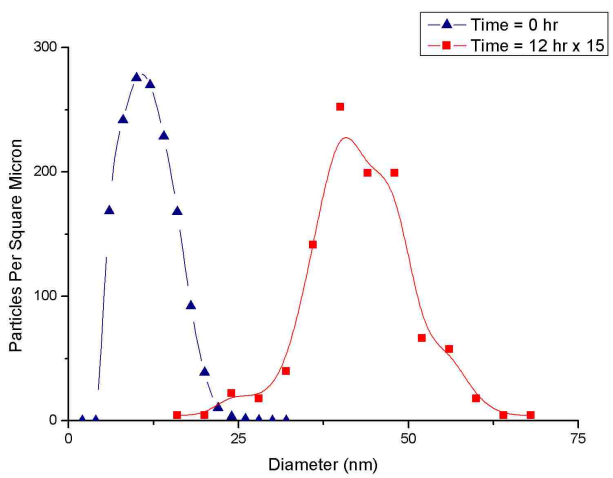

Figure 6.4: Particle size distribution plot of Pd on quartz, plots are from before and after 12 hours of ageing in nitrogen at 900 °C, the aged sample is multiplied by 15 to get the particles per square micron on the same axis to compare the distributions

around 15 nm, may have allowed the migration to occur, which was not seen with the large Pd particles on alumina of studies done by Goeke, et. al. [4] that observed the same region of the sample during the ageing and saw the smaller particles ripen and slowly disappear, my experiments did not allow for those observations of viewing specific particles before and after ageing.

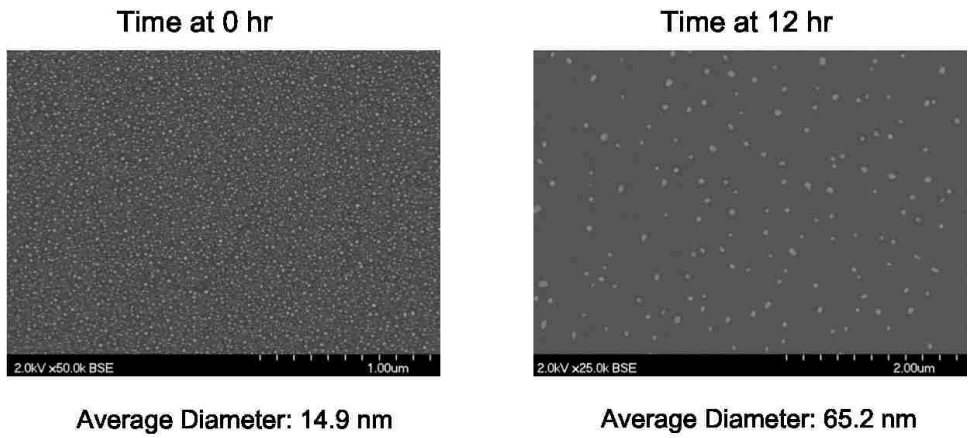

Figure 6.5: High Resolution BSE Scanning Electron Micrographs of Pd on Al_2O_3,initial image (left) and the image taken after 12 hours of ageing in nitrogen at $900\,^{\circ}\mathrm{C}$ (right). Please note, that the images are not taken at the same magnification, the the initial was taken at 50,000X magnification while the aged was taken at half of that, at 25,000X magnification

Comparing all three substrates, Table 6.1, compares how all three substrates sintered under the same conditions. It shows that Pd on YSZ and Pd on quartz sinter about the same amount, with quartz sintering slightly more than YSZ, and with Pd on alumina sintering the greatest. If the sintering rates are high, then it would be speculated that the emission of adatoms were also very high, which would then correlate to the vacuum studies.

However, comparing these sintering results to the results of the $900\,^{\circ}\mathrm{C}$ aged samples in vacuum, shows an opposite trend. The results from the vacuum ageing showed that Pd on alumina evaporated slowest, then Pd on YSZ evaporated the next slowest, and Pd on quartz evaporated the fastest. While the vacuum studies showed Pd on quartz evaporated

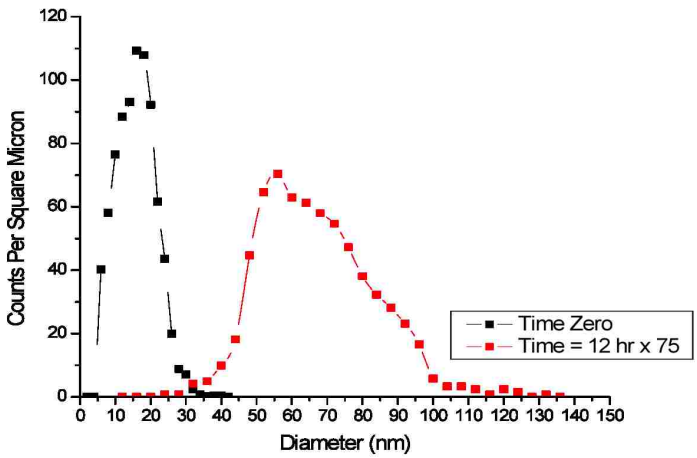

Figure 6.6: Particle size distribution plot of Pd on Al_2O_3, plots are from before and after 12 hours of ageing in nitrogen at $900\,^{\circ}C$, the aged sample is multiplied by 75 to get counts per square micron on the same axis to compare the distributions

the fastest and Pd on alumina evaporated the slowest. If the vacuum results showed the rate of which adatoms are emitted and if ripening, or the emission step, was the dominant mechanism in sintering, then the two observation should correlate with one another. These results do not correlate with one another, an explanation follows in the next section on why these sintering results may not be reliable.

Palladium on Model Supports Aged in N_2 for 12 hr at $900\,^{\circ}C$		
Support	Pd Diameter Before Ageing	Pd Diameter after Ageing
YSZ	11 nm	36 nm
Quartz	11 nm	40 nm
Alumina	15 nm	69 nm

Table 6.1: Average diameter before and after ageing Pd nanoparticles on various supports at $900\,^{\circ}C$ for 12 hours

6.2 Support Modifications and Defects to the Support During Sintering

The results of the previous section are doubted to give reliable results due to some microscopic studies of the substrates. Upon a close microscopic examination of the substrates, defects and other abnormal effects were seen on the support. Any defect or abnormality could enhance or limit the amount of sintering that would be expected to be seen from only the emission mechanism of sintering, invalidating the hypothesis that measuring the emission rates under vacuum will correlate to sintering rates.

The sample of Pd on YSZ had two types of defects present in the sample, one was the tails that were from the grinding of a migrating Pd nanoparticle into the surface. The other defect observed were pits where particles were once present, that at the ageing conditions, the Pd nanoparticles sunk into the substrate. The streaks, as seen in Figure 6.7 left, shows the migration of three different Pd nanoparticles under sintering conditions. From the image, one streak, at the top right portion of the image, with the particle is never in view, another particle, in the center right portion of the screen shows the streak as a fairly small streak, until it turns towards the right, where the particle must have grown much larger as the streak gets much larger. In the center of the figure, a particle is seen to have grown as it crossed the surface, the entire path is shown for this particle. The particle stayed on a similar path and the width of the particle slowly grew as the coalescence and migration events occurred.

The pits, Figure 6.7 right, shows Pd particles and also some black sections to the micrograph, these black sections are believed to be pits where the Pd particles were once before the ageing conditions, during the ageing, the particles burrowed into the surface and then slowly ripened away. This sample, from analyzing the surface with the SEM, displayed both types of sintering, coalescence can be assumed from the streaks and tails and ripening can be assumed from the pit formations.

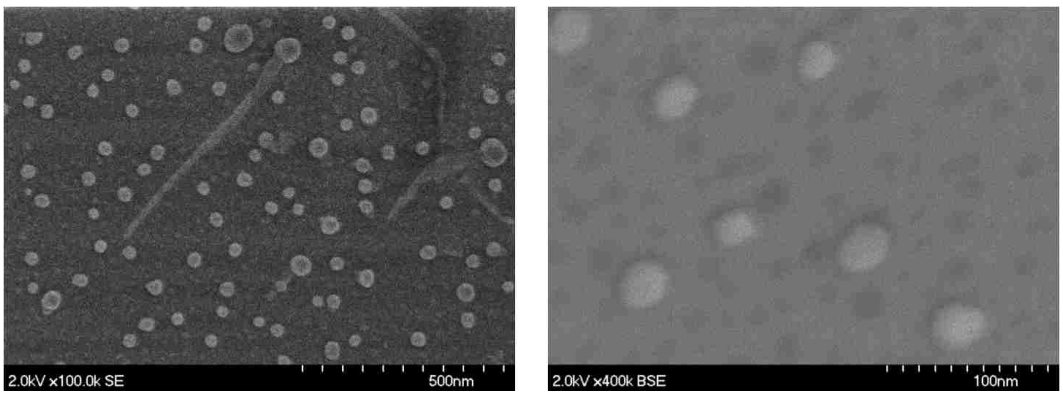

Figure 6.7: Pd on YSZ sample after being aged in nitrogen for 12 hr at $900\,^{\circ}\mathrm{C}$, left, shows three streaks where particles migrated across the surface, right, shows dark regions which are holes from particles that have ripened away

The sample of Pd on quartz, Figure 6.8, reveals small pits on the single crystal surface. If the particles are sinking into the substrate, this limits the amount of adatoms being emitted onto the substrate, an example of this if a 10 nm spherical particle is on the surface and then it sinks 5 nm into the surface, then half of the surface area that could potentially emit adatoms is under the surface. If this pitting is limiting the emission of adatoms, that would greatly decrease the sintering rates. Comparing the sintering rates to the emission rates under vacuum, this would help explain why the sintering rates are so low compared to the enhanced evaporation rates observed on this surface.

In traditional catalyst, it has not been observed that either these tails or pits normally occur, it is not known if this is due to the single crystal substrates or not. The single crystal substrates begin smooth and should be a perfect, defect-free substrate, for these defects to occur, there must be some type of thermal effect or the Pd nanoparticle is binding to the surface and a chemical reaction between the Pd nanoparticle and the surface may cause some of these defects.

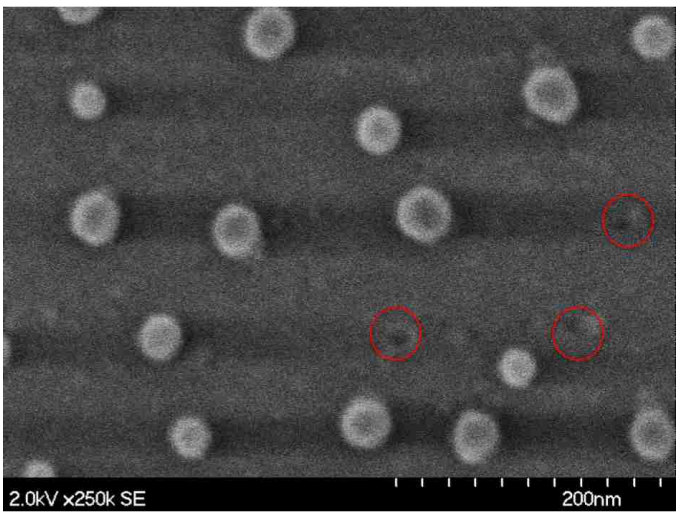

Figure 6.8: Pd on quartz sample after being aged in nitrogen for 12 hr at $900\,^{\circ}\mathrm{C}$ with pits, circled to help see, are from particles that have sunk into the single crystal substrate

6.3 Sintering of Pd Nanoparticles at $700\,^{\circ}\mathrm{C}$

Seeing the defects on the single crystal samples at $900\,^{\circ}\mathrm{C}$, we attempted sintering studies at a lower temperature of $700\,^{\circ}\mathrm{C}$ in hopes to not see any surface defects in the samples after ageing. Evidence has been seen in the literature about noble metals reacting to the metal-oxide at elevated temperatures [29]. A cause for explaining this is the metal becomes liquid-like as it approaches the Tamman temperature, which is usually defined as half of the melting temperature [31].

In Table 6.3, the melting temperatures, T_m, of the materials used in experiments are listed as well as the relative values to the Tamman temperature for each sintering temperature used, $900\,^{\circ}\mathrm{C}$ and $700\,^{\circ}\mathrm{C}$. At $900\,^{\circ}\mathrm{C}$, the Pd value is 0.64 that of the melting temperature, meaning that the Pd nanoparticles are very liquid-like, and when the temperature is lowered to $700\,^{\circ}\mathrm{C}$, the Pd value is lower to being very close to the Tamman temperature, at $0.53T_m$. Even the values of the support decrease significantly, the alumina gets below the Tamman temperature, going from $0.5T_m$ to $0.41T_m$, which should make

the alumina much more stable, and also quartz should be more stable as it is lowered from $0.61T_m$ to $0.50T_m$. Zirconia is also lowered, from $0.39T_m$ to $0.32T_m$, which is below the Tamman temperature at both temperatures.

Melting Temperatures of Materials Used			
Material	Melting Temperature, K	at $900\,^{\circ}\mathrm{C}$	at $700\,^{\circ}\mathrm{C}$
Palladium	1828	$0.64T_m$	$0.53T_m$
Alumina	2345	$0.50T_m$	$0.41T_m$
Silica	1923	$0.61T_m$	$0.50T_m$
Zirconia	2988	$0.39T_m$	$0.32T_m$

Table 6.2: Values of the Melting Temperatures, T_m, of all materials used as well as comparing how close the materials are to the Tamman temperature at each sintering temperature

In response to the defects in the substrate, the samples were never taken to $900\,^{\circ}\mathrm{C}$, including for the initial sample that used the process of VTZ. The new process of creating nanoparticles, as described in earlier sections, was to break up the thin film of Pd in an hydrogen/nitrogen atmosphere at $450\,^{\circ}\mathrm{C}$ for 1 hour. This resulted in particles that were close to the initial sizes created by the VTZ approach, without taking the sample to extreme temperatures where the particles may sink into the substrate.

It is not believed that the surface was damaged under the milder temperatures of $700\,^{\circ}\mathrm{C}$. Examining images of both Pd on YSZ and Pd on quartz after the ageing in N_2, neither support showed any defects, neither tails nor pits. Pd on YSZ, Figure 6.9 left, shows a low magnification view of the sample, for the $900\,^{\circ}\mathrm{C}$, this view included the tails from the particles migrating over the surface, there is no evidence on this sample that tails or migration coalescence events occurred. In Figure 6.9 right, a higher magnification view of the surface after 12 hours of ageing shows that the pits that were observed in the ageing at higher temperatures were no observed at lower temperatures.

And for quartz, Figure 6.10 left, is a low magnification image displaying the surface without any tails or streaks defects. In Figure 6.10 right, shows a high magnification SEM

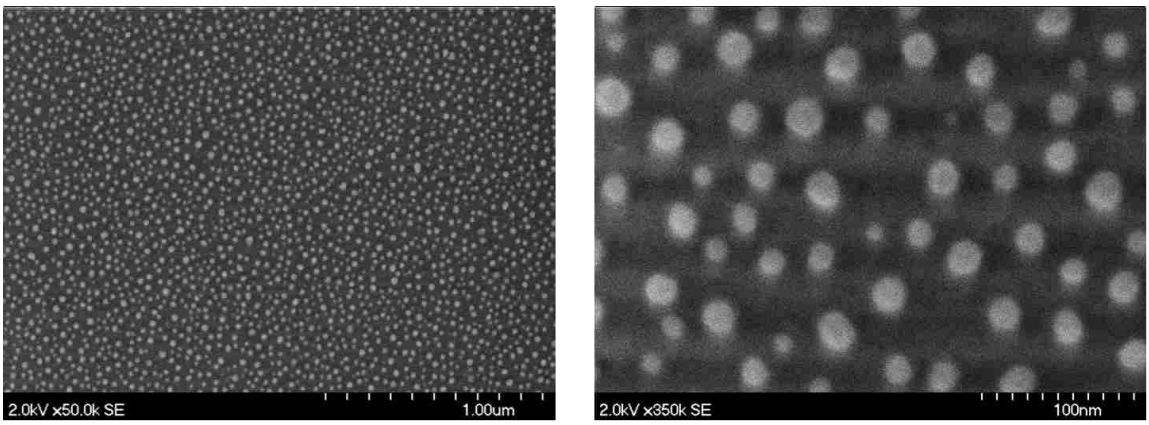

Figure 6.9: High Resolution Scanning Electron Micrographs of Pd on YSZ, a low magnification image (left) does not show any trails in the sample and a much higher magnification (right) does not reveal any pitting from where particles may have sunk into the substrate, both images taken after 12 hours of ageing in nitrogen at $700\,^{\circ}\mathrm{C}$

image of the quartz surface, no pits were seen in the image, as was observed when aged at $900\,^{\circ}\mathrm{C}$ for the same amount of time. The particles do look irregularly shaped with dark centers and a lighter perimeter, this is believed to have occurred as the particles grew under these milder conditions that the particles developed facets and the dark/light regions are occurring due to the different facets having different thickness and the electrons from the beam are being emitted from the particles at different intensities.

Also, sintering will be much slower at $700\,^{\circ}\mathrm{C}$ than at $900\,^{\circ}\mathrm{C}$, this is due to many factors, including the vapor pressure of the metal not being nearly as high and the kinetics of sintering will be much slower at lower temperatures The vapor pressure of Pd at $900\,^{\circ}\mathrm{C}$ is 6.35 x 10^{-8} Torr, while the Pd vapor pressure at $700\,^{\circ}\mathrm{C}$ is three order of magnitudes lower at 4.16 x 10^{-11} Torr. The lower vapor pressure means that there will not be nearly as many adatoms emitted onto the substrate for ripening at $700\,^{\circ}\mathrm{C}$ then at $900\,^{\circ}\mathrm{C}$, which will reduce the amount of sintering considerably.

The Pd on YSZ sample sintered slowly at the elevated temperatures of $900\,^{\circ}\mathrm{C}$, going

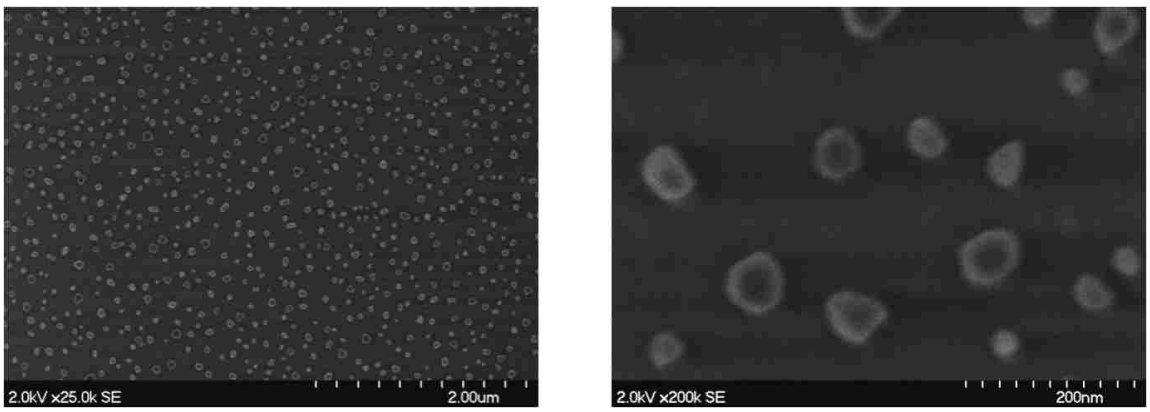

Figure 6.10: High Resolution Scanning Electron Micrographs of Pd on quartz, a low magnification image (left) does not show any trails in the sample and a much higher magnification (right) does not reveal any pitting from where particles may have sunk into the substrate, the particles do look irregularly shaped, possible because the larger particles are faceted, both images taken after 12 hours of ageing in nitrogen at $700\,^{\circ}\mathrm{C}$

from an average diameter of 11 nm to 36 nm. Using the hydrogen reduction process to create an initial particles resulted in particles slightly larger, at an average diameter of 18 nm, Figure 6.11. The sample, over 12 hours of sintering in N_2, grew slightly to an average diameter of 24 nm.

The particle size distribution for Pd on YSZ, Figure 6.12, lost many of it small particles, sized 4 nm to 20 nm during the ageing, this is typical of smaller particles ripening to larger particles, there is a slight peak at very small particles, around 6 nm, which possibly some small particles still present on the sample that haven't ripened away yet. The initial and the aged 12 hours distributions or both Gaussian in appearance, with the aged sample having a slightly broader distribution, but not with an excessive tail compared to the mean, largest particles are larger than 50 nm.

For Pd on quartz sintering at $700\,^{\circ}\mathrm{C}$ in nitrogen, the initial sample had an average diameter of 15 nm, then after 12 hours of sintering, the average diameter increased greatly to 55 nm, Figure 6.13. This compared to what was observed in the sintering for 12 hours at

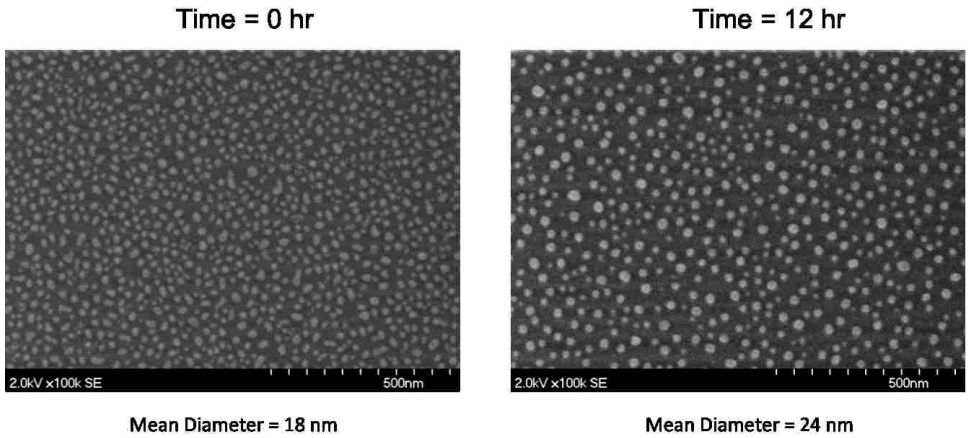

Figure 6.11: High Resolution Scanning Electron Micrographs of Pd on YSZ, initial image (left) and the image taken after 12 hours of ageing in nitrogen at 700 °C (right)

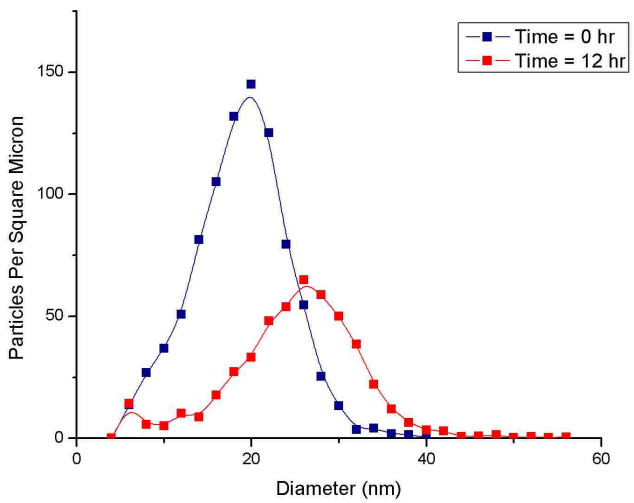

Figure 6.12: Particle size distribution plot of Pd on YSZ, plots are from before and after 12 hours of ageing in nitrogen at 700 °C

900 °C, the average particle size going from 11 nm to 40 nm, also supports the argument that the surface defects in the case of pits hinders the rate of sintering. At a the lower sintering temperature the particle size greatly increased, going to an average particle size of 55 nm, while at a higher sintering temperature, where it would be thought that the higher temperature would increase the sintering rate, actually had a lower average particle size of 40 nm, concluding that these pits that were formed at the higher sintering temperatures are responsible for the lower sintering rate at a much higher temperature. The faster sintering rates also agrees with the evaporation experiments where the rate of Pd on quartz greatly exceeded what would normally be predicted by direct evaporation and faster than any other supported Pd.

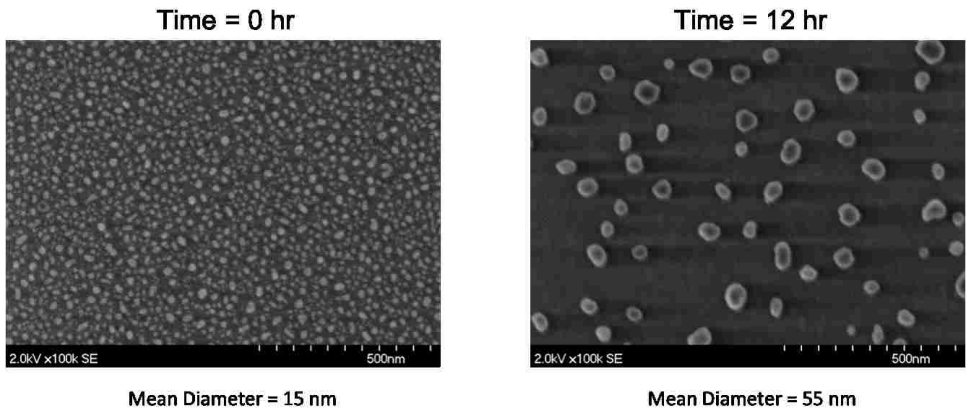

Figure 6.13: High Resolution Scanning Electron Micrographs of Pd on quartz, initial image (left) and the image taken after 12 hours of ageing in nitrogen at 700 °C (right)

The particle size distribution of the Pd on quartz sample, Figure 6.14, starts off Gaussian in the initial distribution. As the sample is aged, the particle size distribution shifts to larger particles with a Gaussian like distribution centered around the mean of 55 nm, the smallest particles are around 20 nm with the largest particles well over 110 nm, twice the mean. Growth of particles to over diameters of over 100 nm after ageing from the initial sample that had the largest particles less than 50 nm in diameter shows that Pd on quartz

is not a very stable catalyst and that it sinters rapidly.

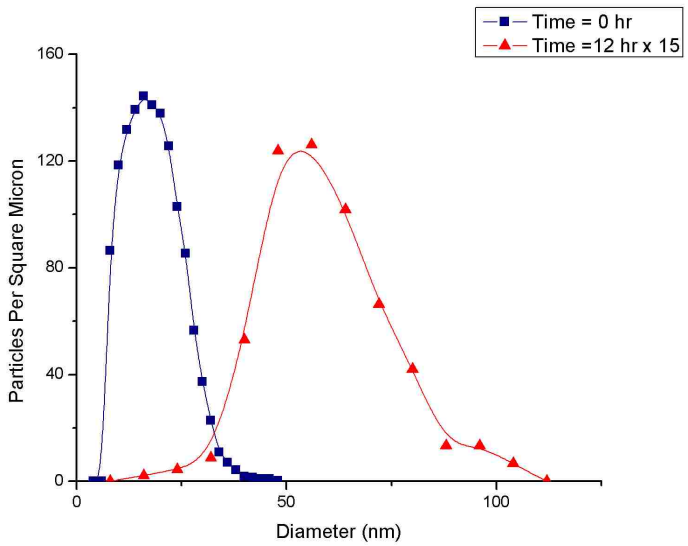

Figure 6.14: Particle size distribution plot of Pd on quartz, plots are from before and after 12 hours of ageing in nitrogen at $700\,^{\circ}\mathrm{C}$, the aged sample is multiplied by 15 to get the particles per square micron on the same axis to compare the distributions

The Pd on alumina samples, which sintered the most at $900\,^{\circ}\mathrm{C}$, did not sinter as rapidly under the milder temperature of $700\,^{\circ}\mathrm{C}$. The initial particles were on average around 15 nm in diameter, Figure 6.15, after 12 hours under N_2 at $700\,^{\circ}\mathrm{C}$, the average diameter increased only to an average diameter of 20 nm. The alumina is much more stable at $700\,^{\circ}\mathrm{C}$ than at $900\,^{\circ}\mathrm{C}$, comparing to the Tamman temperature, the temperature at which a solid will start acting like a liquid or half of the melting temperature, alumina is at the Tamman temperature at $900\,^{\circ}\mathrm{C}$, $0.5T_m$, while at $700\,^{\circ}\mathrm{C}$ it is under the Tamman temperature, $0.41T_m$. Also, the work by Tomsia [29], did not report any unusual behavior at temperatures this low on alumina, which also may increase the stability of the Pd on the alumina surface which will in turn prevent sintering due to abnormalities that are forming on the surface from the interaction with the Pd nanoparticle.

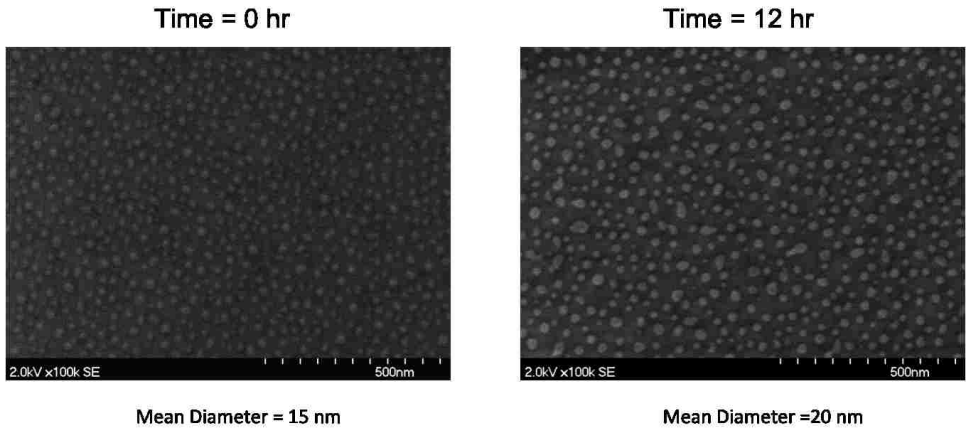

Figure 6.15: High Resolution Scanning Electron Micrographs of Pd on alumina, initial image (left) and the image taken after 12 hours of ageing in nitrogen at $700\,^{\circ}\mathrm{C}$ (right)

Plotting the particle size distribution of the initial and aged nanoparticles, Figure 6.16, shows that overall shape of the distribution remains fairly the same shape. There is a large decrease in particles that are less than 20 nm from the initial sample and there is a slight increase in particles that are larger than 30 nm after ageing from the initial sample. However, a sintering mechanism cannot be concluded from this distribution, it may be assumed that the smaller particles are loosing mass to the the larger particles, which results in the sharp decrease of smaller particles and this also explains why there is only a slight increase in the larger particles and not such a dramatic increase in the sizes of the large particles which would be typical of the coalescence events.

Comparing the sintering results from $700\,^{\circ}\mathrm{C}$, Table 6.3, to the sintering results at $900\,^{\circ}\mathrm{C}$, Table 6.1, shows that the sintering results are not consistent between the two temperatures. At $900\,^{\circ}\mathrm{C}$, the Pd on alumina sinters the fastest, with Pd on quartz and Pd on YSZ sintering not as much, while for the $700\,^{\circ}\mathrm{C}$, Pd on quartz sintering the greatest, with Pd on YSZ and Pd on alumina sintering only slightly. The results at $900\,^{\circ}\mathrm{C}$ were questioned due to the surface defects that were created at the high temperatures, Pd nanoparticles burrowing into the substrate on quartz and YSZ and the tails that formed

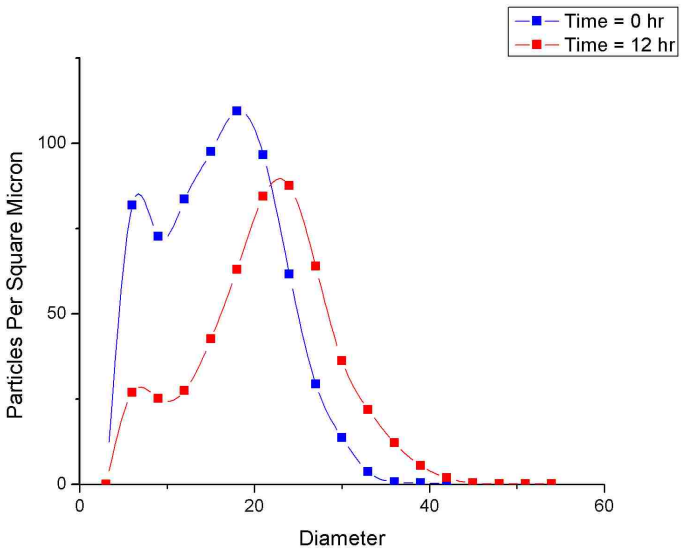

Figure 6.16: Particle size distribution plot of Pd on alumina, plots are from before and after 12 hours of ageing in nitrogen at 700 °C

on YSZ support, which may limit the amount of sintering that should have been observed and the work of Tomsia [29] which detailed that a surface reaction of Pd on alumina may cause defects on the alumina substrate, which would account for the enhanced sintering rate observed.

The sintering experiments at 700 °C revealed that at the lower temperature, that the defects on the substrate were not observed, which would allow for sintering on a more idealized surface where adatoms of the whole particle could be emitted and received from the surface where ripening would be the dominant mechanism without any obstacles to overcome. These results showed that Pd on quartz would sinter the most, the burrowing of the Pd nanoparticles at the elevated temperature did cause for a decrease of sintering of Pd. The sample of Pd on alumina sintered the least, the lower temperature was not favorable for the Pd nanoparticle to react with the alumina surface, and Pd on YSZ sintered just slightly more than the Pd on alumina sample.

Palladium on Model Supports Aged in N_2 for 12 hr at $700\,^{\circ}\mathrm{C}$		
Support	Pd Diameter Before Ageing	Pd Diameter after Ageing
YSZ	18 nm	24 nm
Quartz	15 nm	55 nm
Alumina	15 nm	20 nm

Table 6.3: Average diameter before and after ageing Pd nanoparticles on various supports at $700\,^{\circ}\mathrm{C}$ for 12 hours

Chapter 7

Conclusions and Future Work

From this work, it was shown that the emission rates of palladium (Pd) particles on different metal-oxide model supports under a vacuum atmosphere at elevated temperatures can be related to the rates of sintering. In this study, Pd nanoparticles between 10 and 20 nm were created on three different single crystal, metal-oxide support, sapphire or α-alumina (0001), yttria stabilized zirconia (YSZ) (100), and quartz or silica (x plane out). These model catalyst systems were then either aged in vacuum, to measure the emission rates, or aged in nitrogen, to measure the sintering rates.

The experiments done under high vacuum conditions were conducted at $900\,^{\circ}\mathrm{C}$ for 30 minute increments. After the ageing, the samples were removed from the vacuum and imaged with a scanning electron microscope (SEM), from the analysis of these images, the particle sizes and from the sizes the mass of the system and particle size distribution could be calculated. From the change of the calculated mass, the evaporation or emission rate could be calculated. Experimentally, the highest evaporation rate for a Pd/metal-oxide system was Pd/quartz, followed by Pd/YSZ, with the slowest evaporation rate for Pd/alumina.

For the evaporation system, deterministic models based on direct evaporation theory

and Monte Carlo Simulations were used to examine the experimental data. The deterministic model of direct evaporation was calculated for each initial distribution to compare how the system would evaporate if only direct evaporation was occurring. From this result, it was shown that Pd/YSZ evaporated very similar in mass loss to the direct evaporation model, while Pd/quartz evaporated much faster than would expected from direct evaporation only and Pd/alumina evaporated slower than would be expected from direct evaporation.

These results helped explain the mechanism of evaporation for each support.

1. For Pd/YSZ it appeared that evaporation was occurring directly from the particles, but when the particle size distribution of the experiments were compared to the direct evaporation calculations, the experimental distribution contained larger particles. This meant that adatoms were being emitted from the particles onto the substrate and ripening was occurring during evaporation.
2. For Pd/quartz the enhanced evaporation rate was from the evaporation of adatoms from the particle and from the support.
3. The only explanation that would explain why Pd/alumina had slower evaporation came from the literature, that at such high temperatures, the Pd and the alumina surface was forming a type of alloy where the Pd would not easily evaporate.

These macroscopic observations were confirmed with the help of a focused ion beam (FIB) etching out a grid on the YSZ substrate so individual particles could be monitored during the evaporation process. From these observations, it was clear that on the YSZ support that particles did ripen under the vacuum conditions. That at $900\,^{\circ}\mathrm{C}$, the Pd nanoparticles on YSZ did evaporate but larger particles would sustain their mass much longer due to the ripening of smaller particles, and one particle that was observed did grow in size after 0.5 hr of vacuum ageing. This microscopic view of evaporation confirms the mechanism of evaporation for Pd/YSZ from the macroscopic studies.

Sintering studies under nitrogen performed at $900\,^{\circ}\mathrm{C}$ for 12 hrs on these substrates did not show that the evaporation rates and sintering rates correlated. The sintering rates showed that Pd/alumina sintered the most, with Pd/quartz and Pd/YSZ sintering about equally with rates much slower than the Pd/alumina sample. However, the support did show signs of defects after the ageing, the samples of Pd/YSZ showed trails where the particles had migrated across the surface and also pits where particles had burrowed down into the support. The sample of Pd/quartz also showed signs of pits where particles had sunk into the substrate. These support defects made the sintering rates questionable, since these phenomena have not been observed on traditional catalyst supports, and experiments were planned to look at sintering rates at a lower temperature.

Sintering studies performed at $700\,^{\circ}\mathrm{C}$ for 12 hrs in nitrogen on these substrates did not show any surface defects that were present in the $900\,^{\circ}\mathrm{C}$ experiments. These results showed that Pd/quartz sintered the most, with Pd/YSZ sintering some while Pd/alumina didn't sinter much at all and was fairly stable. With no surface defects, these results were not influenced by any extra factors from the support. These results are also the same as the evaporation data at $900\,^{\circ}\mathrm{C}$.

These experiments showed that by measuring the evaporation rate of metal nanoparticles on model supports, that sintering rates can be predicted by which catalyst might be the most stable. Future work for these studies include studying the effect of alloys on evaporation rates, whether or not a second metal species will have a role in the vapor pressure of the nanoparticle. Also, work on a model for predicting catalyst system could be developed in a fundamental property of the metal and support could established to predict sintering rates.

References

[1] A. K. Datye, Q. Xu, K. C. Kharas, and J. M. McCarty, "Particle size distributions in heterogeneous catalysts: What do they tell us about the sintering mechanism?," *Catalysis Today*, vol. 111, pp. 59–67, 2006.

[2] I. Lifshitz and V. Slyozo, "The kinetics of precipitation from supersaturated solid solutions," *Journal of Physics and Chemistry of Solids*, vol. 19, no. 1-2, pp. 35–50, 1961.

[3] C. Wagner, "heorie dealtering von niederschlägen durch umlösen," *Berichte der Bunsengesellschaft für Physikalische Chemie*, vol. 65, 1961.

[4] R. S. Goeke and A. K. Datye, "Model oxide supports for studies of catalyst sintering at elevated temperatures," *Topics in Catalysis*, vol. 46, no. 1–2, pp. 3–9, 2007.

[5] I. Chorkendorff and J. Niemantsverdriet, *Concepts of modern catalysis and kinetics*. Wiley-VCH, 2007.

[6] G. B. McVicker, R. L. Garten, and R. T. K. Baked, "Surface area stabilization of Ir/Al_20_3 catalysts by CaO, SrO, and BaO under oxygen atmospheres: Implications on the mechanism of catalyst sintering and redispersion," *Journal of Catalysis*, vol. 54, pp. 129–142, 1978.

[7] P. Wynblatt and N. Gjostein, "Supported metal crystallites," *Solid State Chemistry*, vol. 9, pp. 21–58, 1975.

[8] C. Granqvist and R. Buhrman, "Ultrafine metal particles," *Journal of Applied Physics*, vol. 47, p. 2200, May 1976.

[9] F. Yang, M. S. Chen, and D. W. Goodman, "Sintering of Au particles supported on TiO_2(110) during CO oxidation," *J. Phys. Chem. C*, vol. 113,, no. 1, pp. 254–260, 2009.

[10] R. Liu, P. Crozier, C. Smith, D. Hucul, J. Blackson, and G. Salaita, "Metal sintering mechanisms and regeneration of palladium/alumina hydrogenation catalysts," *Applied Catalysis A: General*, vol. 282, pp. 111–121, 2005.

[11] J. P. Gabaldon, M. Bore, and A. K. Datye, "Mesoporous silica supports for improved thermal stability in supported Au catalysts," *Topics in Catalysis*, vol. 44, p. 253, June 2007.

[12] C. H. Bartholomew and W. L. Sorensen, "Sintering kinetics of silica and alumina-supported nickel in hydrogen atmosphere," *Journal of Catalysis*, vol. 81, pp. 131–141, 1983.

[13] I. Langmuir, "The vapor pressure of metallic tungsten," *The Physical Review*, vol. 2, no. 5, pp. 329–342, 1913.

[14] N. D. Lisgarten, J. R. Sambles, and L. M. Skinner, "Vapour pressure over curved surfaces-the Kelvin equation," *Contemporary Physics*, vol. 12, no. 6, pp. 575–593, 1971.

[15] Y. Kaganovskii, D. Beke, and S. Yurchenko, "Kinetics of evaporation of beaded thin films," *Surface Science*, vol. 319, pp. 207–218, 1994.

[16] A. Imre, E. Gontier-Moya, D. Beke, and B. Ealet, "Auger electron spectroscopy of the kinetics of evaporation of palladium beaded films from sapphire substrate," *Applied Physics A Matterials Science & Processing*, vol. 67, pp. 469–473, 1998.

[17] D. W. Goodman and J. Houston, "Catalyst: New perspectives from surface science," *Science*, vol. 236, pp. 403–409, April 1987.

[18] M. Valden, X. Lai, and D. W. Goodman, "Onset of catalytic activity of gold clusters on titania with the appearance of nonmetallic properties," *Science*, vol. 281, pp. 1647–1650, Septemeber 1998.

[19] M. S. Chen and D. W. Goodman, "The structure of catalytically active gold on titania," *Science*, vol. 306, pp. 252–255, October 2004.

[20] J. A. Rodriguez and D. W. Goodman, "The nature of the metal-metal bond in bimetallic surfaces," *Science*, vol. 257, no. 5072, pp. 897–903, 1992.

[21] M. Chen, D. Kumar, C.-W. Yi, and D. W. Goodman, "The promotional effect of gold in catalysis by palladium-gold," *Science*, vol. 310, pp. 291–293, October 2005.

[22] F. Gao, S. McClure, Y. Cai, K. Gath, Y. Wang, M. Chen, Q. Guo, and D. Goodman, "CO oxidation trends on Pt-group metals from ultrahigh vacuum to near atmospheric pressures: A combined in situ PM-IRAS and reaction kinetics study," *Surface Science*, vol. 603, pp. 65–70, 2009.

[23] F. Gao, Y. Wang, Y. Cai, and D. W. Goodman, "CO oxidation on Pt-group metals from ultrahigh vacuum to near atmospheric pressures. 2. Palladium and Platinum," *Journal of Physical Chemistry C*, vol. 113, pp. 174–181, 2009.

[24] S. M. McClure, M. Lundwall, F. Yang, Z. Zhou, and D. W. Goodman, "CO oxidation on $Rh/SiO_2/Mo(112)$ model catalysts at elevated pressures," *Journal of Physical Chemistry C*, vol. 113, pp. 9688–9697, 2009.

[25] S. M. McClure, M. Lundwall, Z. Zhou, F. Yang, and D. W. Goodman, "Characterization of Pt/SiO_2 model catalysts at UHV and near atmospheric pressures," *Catalysis Letters*, vol. 133, pp. 298–306, 2009.

[26] D. E. Starr, D. J. Bald, J. E. Musgrove, J. T. Ranney, and C. T. Campbell, "Microcalorimetric measurements of the heat of adsorption of Pb on well-defined oxides: MgO(100) and p(2x1)-oxide on Mo(100)," *Journal of Chemical Physics*, vol. 114, no. 8, pp. 3752–3764, 2001.

[27] C. T. Campbell, S. C. Parker, and D. E. Starr, "The effect of size-dependent nanoparticle energetics on catalyst sintering," *Science*, vol. 298, p. 811, 2002.

[28] S. C. Parker and C. T. Campbell, "Kinetic model for sintering of supported metal particles with improved size-dependent energetics and applications to Au on TiO_2 (110)," *Physical Review B*, vol. 75, no. 035430, 2007.

[29] E. Saiz, R. M. Cannon, and A. P. Tomsia, "High-temperature wetting and the work of adhesion in metal/oxide systems," *Annual Review of Materials Research*, vol. 38, pp. 197–226, 2008.

[30] A. Bellare, D. B. Dadyburjor, and M. J. Kelley, "Evolution of bimodal distributions in the sintering of model supported metal catalysts," *Journal of Catalysis*, vol. 117, pp. 78–90, May 1989.

[31] J. Moulijn, A. van Diepen, and F. Kapteijn, "Catalyst deactivation: is it predictable? What to do?," *Applied Catalysis A: General*, vol. 212, pp. 3–16, 2001.